

Tracing the origin of the AGN fuelling reservoir in MCG–6-30-15[★]

S. I. Raimundo,^{1†} R. I. Davies,² R. E. A. Canning,^{3,4} A. Celotti,^{5,6,7} A. C. Fabian⁸
and P. Gandhi⁹

¹*Dark Cosmology Centre, Niels Bohr Institute, University of Copenhagen, DK-2100 Copenhagen Ø, Denmark*

²*Max-Planck-Institut für extraterrestrische Physik, Postfach 1312, D-85741 Garching, Germany*

³*Kavli Institute for Particle Astrophysics and Cosmology (KIPAC), Stanford University, 452 Lomita Mall, Stanford, CA 94305-4085, USA*

⁴*Department of Physics, Stanford University, 452 Lomita Mall, Stanford, CA 94305-4085, USA*

⁵*SISSA – Scuola Internazionale Superiore di Studi Avanzati, Via Bonomea 265, I-34135 Trieste, Italy*

⁶*INFN – Sezione di Trieste, via Valerio 2, I-34127 Trieste, Italy*

⁷*INAF – Osservatorio Astronomico di Brera, via Bianchi 46, I-23807 Merate, Italy*

⁸*Institute of Astronomy, University of Cambridge, Madingley Road, Cambridge CB3 0HA, UK*

⁹*Department of Physics and Astronomy, University of Southampton, Highfield, Southampton SO17 1BJ, UK*

Accepted 2016 October 11. Received 2016 October 10; in original form 2016 August 3

ABSTRACT

The active galaxy MCG–6-30-15 has a 400 pc diameter stellar kinematically distinct core, counter-rotating with respect to the main body of the galaxy. Our previous high spatial resolution (0.1 arcsec) *H*-band observations of this galaxy mapped the stellar kinematics and [Fe II] 1.64 μm gas dynamics though mainly restricted to the spatial region of the counter-rotating core. In this work, we probe the stellar kinematics on a larger field of view and determine the ionized and molecular gas dynamics to study the formation of the counter-rotating core and the implications for active galactic nucleus (AGN) fuelling. We present integral field spectroscopy observations with SINFONI in the *H* and *K* bands in the central 1.2 kpc and with VIMOS HR-blue in the central 4 kpc of the galaxy. Ionized gas outflows of $v_{\text{out}} \sim 100 \text{ km s}^{-1}$ are traced by the [Ca VIII] 2.32 μm coronal line and extend out to at least a radius of $r \sim 140 \text{ pc}$. The molecular gas, traced by the H₂ 2.12 μm emission, is also counter-rotating with respect to the main body of the galaxy, indicating that the formation of the distinct core was associated with inflow of external gas into the centre of MCG–6-30-15. The molecular gas traces the available gas reservoir for AGN fuelling and is detected as close as $r \sim 50\text{--}100 \text{ pc}$. External gas accretion is able to significantly replenish the fuelling reservoir suggesting that the event which formed the counter-rotating core was also the main mechanism providing gas for AGN fuelling.

Key words: galaxies: active – galaxies: individual: MCG–6-30-15 – galaxies: kinematics and dynamics – galaxies: nuclei – galaxies: Seyfert.

1 INTRODUCTION

The observed correlations between properties of supermassive black holes and their host galaxies (Magorrian et al. 1998; Ferrarese & Merritt 2000; Gebhardt et al. 2000; Marconi & Hunt 2003; Häring & Rix 2004) suggest a co-evolution in which the active galactic nucleus (AGN) phase may play a central role in regulating gas accretion and star formation in the galaxy. Understanding how the host galaxy fuels the AGN and how the AGN in turn affect gas

accretion is currently one of the most important questions in AGN and galaxy evolution studies.

To understand the physics of AGN fuelling, it is essential to study not only the black hole accretion physics but also the environment of the host galaxies, in particular their central regions. Due to the higher spatial resolution achievable, several signatures of fuelling have been observed in the low-redshift Universe, providing the best laboratory to study AGN fuelling. The molecular gas survey Nuclei of GALaxies (NUGA) for example has found a wide variety of fuelling tracers on the form of dynamical perturbations in the range 0.1–1 kpc in lower luminosity AGN (Seyferts and low-ionization nuclear emission-line regions, LINERs; e.g. García-Burillo et al. 2003; García-Burillo & Combes 2012). The ionized gas in the central kiloparsec also seems to be more disturbed in Seyfert host galaxies than in inactive galaxies (Dumas et al. 2007). For even smaller physical scales, Hicks et al. (2013) and Davies et al. (2014)

[★] Based on observations collected at the European Organisation for Astronomical Research in the Southern hemisphere, Chile, during programme 093.B-0734 and on observations made with ESO Telescopes at the La Silla Paranal Observatory under programme 073.B-0617.

† E-mail: s.raimundo@dark-cosmology.dk

compared five pairs of matched active and inactive galaxies at a resolution of ~ 50 pc using infrared integral field spectroscopy. They found that at the scales of $< 200\text{--}500$ pc, where the dynamical time approaches the AGN activity time-scale, there are systematic differences between properties of stars and gas for active and inactive galaxies, associated with the black hole fuelling process. The active galaxies in their sample show a nuclear structure in stars and gas, composed of a relatively young stellar population and of a significant gas reservoir, which could contribute to fuel the black hole. This nuclear structure is not observed in the quiescent galaxies. The presence of circumnuclear discs of molecular gas seems to be required for nuclear activity, with gas inflows and outflows being detected only in active galaxies. Gas inflow/outflow structures are commonly detected in the inner regions of AGN host galaxies (e.g. Storchi-Bergmann et al. 2007; Davies et al. 2009, 2014; Müller-Sánchez et al. 2011), and usually most of the inflow and outflow mass is in the form of molecular gas. At higher spatial resolution, the Atacama Large Millimeter/submillimeter Array has also provided a new view of the small spatial scales around the AGN, with tracers of molecular gas inflow and outflow being detected in most of the AGN observed (e.g. Combes et al. 2013, 2014; García-Burillo et al. 2014; Smajić et al. 2014). Considering the recent work in this field, it has become clear that the central hundreds of parsecs of galaxies are essential to understand the AGN fuelling process.

The S0 galaxy MCG–6–30–15 is a narrow-line Seyfert 1 galaxy, with an AGN luminosity of $L_X(2\text{--}10\text{ keV}) \sim 4 \times 10^{42}$ erg s $^{-1}$ (Vasudevan et al. 2009; Winter et al. 2009) and a total bolometric luminosity of $\sim 3 \times 10^{43}$ erg s $^{-1}$ (Lira et al. 2015). This galaxy has been particularly targeted by X-ray studies, since it was the first source for which the broadened Fe K α emission line was observed, showing that this line was being emitted from the very inner regions of the accretion disc (Tanaka et al. 1995). Our study of the inner 500 pc of MCG–6–30–15 in Raimundo et al. (2013) was the first integral field spectroscopy study on this galaxy. Due to the unprecedented spatial resolution reached (0.1 arcsec ~ 16 pc in the H band), we discovered a previously unknown stellar kinematically distinct core (KDC) in the centre of MCG–6–30–15 counter-rotating with respect to the main body of the galaxy. We first estimated a size of $R \sim 125$ pc for the distinct core due to the limited field of view of our initial observations; we will show in this work that the distinct core has a size of $R \sim 200$ pc. The age of the stars in the counter-rotating core was estimated to be < 100 Myr (Raimundo et al. 2013), which is in line with the findings of Bonatto et al. (2000), who determined that > 35 per cent of the stellar population is the result of bursts of star formation distributed in age between 2.5 and 75 Myr.

Stellar KDCs such as the one in MCG–6–30–15 are characterized by the presence of a stellar core with kinematics and angular momentum distinct from the main body of the galaxy. KDCs can be defined by an abrupt change of more than 30 deg in the local kinematic orientation of the galaxy (e.g. McDermid et al. 2006; Krajnović et al. 2011), with counter-rotating cores having angles of 180 deg. The ATLAS 3D project found that KDCs are present in a small fraction (~ 7 per cent) of early-type galaxies (Krajnović et al. 2011), and seem to be more common in slow rotators than in fast rotators (Emsellem et al. 2011). In spiral galaxies, stellar counter-rotating discs are present in < 8 per cent of the galaxies and are rarer than counter-rotating gas discs (< 12 per cent; Pizzella et al. 2004). In S0 galaxies such as MCG–6–30–15, it is estimated that < 10 per cent host counter-rotating stars (Kuijken, Fisher & Merrifield 1996) and $\sim 25\text{--}40$ per cent host a counter-rotating gas disc (Kuijken et al. 1996; Kannappan & Fabricant 2001; Pizzella et al. 2004; Bureau & Chung 2006), or ~ 70 per cent if consider-

ing isolated galaxies (Katkov, Sil’chenko & Afanasiev 2014) which is consistent with an external origin for the counter-rotating gas (Bertola, Buson & Zeilinger 1992). Pizzella et al. (2004) argue that the formation of counter-rotating gas discs is favoured in S0 galaxies due to their low gas fraction. In spiral galaxies which are more gas rich, the acquired external gas can be swept away due to the interactions with the pre-existing gas which would make the counter-rotating disc observable only when its mass is higher than the one of the pre-existing gas. The difference between the fraction of S0 galaxies with observed counter-rotating gas and observed counter-rotating stars may be due to the inherent difficulty of detecting small numbers of counter-rotating stars (e.g. Bureau & Chung 2006).

The presence of large kinematic misalignments of counter-rotating gas, in particular in S0 galaxies, has been taken as strong evidence of the external origin of the gas (e.g. Bertola et al. 1992; Davis & Bureau 2016). If the gas originates from stellar mass loss in the galactic disc, then stars and gas are expected to corotate. Internal physical processes such as weak bars or spirals can cause mild kinematic misalignments between gas and stars (up to an angular difference $\Delta \text{PA} \lesssim 55$ deg; Dumas et al. 2007). However, large kinematic misalignments or counter-rotating gas ($\Delta \text{PA} = 180$ deg) would require a significant amount of energy to change the angular momentum of the corotating gas, which is unlikely to be provided by internal processes, especially for large gas masses (e.g. Dumas et al. 2007; Davies et al. 2014). Simulations of internal dynamical perturbations, for example of nuclear spirals generated by asymmetries in the galactic potential (Maciejewski 2004) or gas flow in barred spiral galaxies (Regan, Sheth & Vogel 1999), do not seem to generate counter-rotating gas structures.

The main theories for the formation of KDCs involve the inflow of material (stars/gas) with a distinct angular momentum into the centre of the galaxy. However, there is more than one mechanism than can drive this material inwards to produce the KDCs and can result in two different KDC populations. In optical wavelengths, McDermid et al. (2006) found that there is one population of KDCs which are typically large (diameter ≥ 1 kpc) with old stellar populations (age ≥ 10 Gyr) found in slow-rotating early-type galaxies. In this case, the stellar population within the KDC and in the main body of the galaxy show little or no difference. This can be explained if the distinct core was formed a long time ago and the differences in origin have already been diluted or if the KDC is a superposition of stellar orbits and caused by the geometry of the galaxy. It has been suggested (e.g. Hernquist & Barnes 1991) and shown from simulations (Bois et al. 2011; Tsatsi et al. 2015) that these large KDCs can be formed by high mass ratio mergers (1:1 or 2:1) between disc galaxies with prograde or retrograde orbits. A non-merger scenario has also been suggested from simulations, where counter-rotating stellar discs are formed early in the history of the galaxy from the infall of gas with misaligned spin through large-scale filaments (Algorry et al. 2014). The second population of KDCs found by McDermid et al. (2006) consists of smaller structures (diameter < 1 kpc), found mostly in fast rotators, typically close to counter-rotating in relation to the outer parts of the galaxy and showing younger stellar populations. These KDCs were likely formed by recent accretion of gas which then formed stars *in situ*. The fact that the distinct core has an angle $\text{PA}_{\text{kin}} \sim 180^\circ$ in relation to the outer parts of the galaxy may indicate that in fact dissipation processes are important in the formation of these smaller KDCs.

MCG–6–30–15 is one of the galaxies with higher AGN luminosity among the galaxies with known stellar distinct cores, and therefore we are interested in understanding the impact which the formation

of the KDC may have on AGN fuelling. Davies et al. (2014) studied a sample of S0 galaxies and found that the ones with AGN typically have gas detected on large scales (> 1 kpc), while the inactive ones do not. They also find a fraction of sources with counter-rotating gas consistent with what is expected for external accretion. These observations suggest that in S0 galaxies, AGN are typically fuelled by external accretion. They have also shown that in two of the galaxies they observed (IC 5267 and NGC 3368), the external counter-rotating gas can reach the inner tens of parsecs of the galaxy.

In our previous work (Raimundo et al. 2013), we studied the stellar kinematics out to $r < 250$ pc in MCG–6-30-15. Since our data were limited to the H band and to a $3 \text{ arcsec} \times 3 \text{ arcsec}$ field of view, we only had one tracer for the ionized gas on the form of [Fe II] 1.64 μm emission, mainly restricted to the spatial region of the counter-rotating core. In the present work, our goal is foremost to probe the dynamics of the molecular gas, for which there are no previous observations. In this work, we will investigate if the formation of the counter-rotating core is associated with inflow of gas into the central regions of the galaxy and if this gas can create or replenish the molecular gas reservoir for AGN fuelling. We will first describe the SINFONI and VIMOS observations and the data reduction and analysis. We will then present the results on the stellar, ionized and molecular gas properties in the galaxy. Using the stellar and gas dynamics, we set new constraints on the black hole mass. Finally, we will discuss, based on these observations, the origin of the stellar counter-rotating core and its effect on AGN fuelling.

We adopt the standard cosmological parameters of $H_0 = 70 \text{ km s}^{-1} \text{ Mpc}^{-1}$, $\Omega_m = 0.27$ and $\Omega_\Lambda = 0.73$. The scale for our measurements is approximately $0.158 \text{ kpc arcsec}^{-1}$ at a redshift $z = 0.0077$ (Fisher et al. 1995 value quoted at the NASA/IPAC Extragalactic Database). The distance to MCG–6-30-15 used in this paper is 33.2 Mpc (Wright 2006).

2 DATA ANALYSIS

2.1 SINFONI data reduction

The SINFONI/VLT H -band data with $R \sim 3000$ were taken on the night of 2014 June 2 with a pixel scale of $0.25 \text{ arcsec} \times 0.125 \text{ arcsec}$, sampling a field of view of $8 \text{ arcsec} \times 8 \text{ arcsec}$. Each exposure was of 300 s, in an object (O) and sky (S) sequence of OSO. The total on-source exposure time was 55 min. The SINFONI/VLT K -band data with $R \sim 4000$ were taken on four nights (2014 June 4, 12 and July 2, 3) with a pixel scale $0.25 \text{ arcsec} \times 0.125 \text{ arcsec}$ and also sampling a field of view of $8 \text{ arcsec} \times 8 \text{ arcsec}$. Each exposure was of 300 s, in an object (O) and sky (S) sequence of OSO. The total on-source exposure time was 2 h 30 min. The data reduction was done with the European Southern Observatory (ESO) pipeline for SINFONI ESOREX version 3.10.2 and complemented with independent IDL routines. The two main extra routines used were the implementation of the sky emission subtraction described in Davies et al. (2007) and a bad pixel removal routine for 3D data cubes (Davies et al. 2010) – a 3D version of LA cosmic (van Dokkum 2001). For the analysis, the cubes were shifted considering the offsets recorded in their headers, combined and re-sampled to a spatial scale of $0.125 \text{ arcsec} \times 0.125 \text{ arcsec}$. The observations were taken with a rotation angle of 25 deg to obtain a better spatial sampling along the major axis of the galaxy. In the plots in this paper, the x -axis will be parallel to the major axis of the galaxy. The compass in each of the plots indicates the relative position in the sky. A more detailed description of the typical data reduction steps for the H band can be found in Raimundo et al. (2013).

The point spread function (PSF) is determined from the intensity of the broad component of the atomic hydrogen Brackett recombination lines. The broad-line region where these lines are produced is unresolved in our observations and therefore the line width of the broad hydrogen emission provides a method to estimate the PSF. Several transitions of this Brackett series are observed both in the H and K bands. In the H band, there are five strong lines which we use to measure the PSF and also later in this section to remove the AGN contribution from the spectra. In the K band, we use the strongest line of the $(7-4) \lambda = 2.166 \mu\text{m}$ transition ($\text{Br}\gamma$). We fit these lines with a double Gaussian (one narrow Gaussian to model the core and one broader Gaussian to model the extended emission), to empirically model the PSF. The full width half-maximum of each of the Gaussians is for the H band ($\text{FWHM} = 3.6 \text{ pixels} \sim 0.4 \text{ arcsec}$) and ($\text{FWHM} = 6.7 \text{ pixels} \sim 0.8 \text{ arcsec}$) and for the K band ($\text{FWHM} = 3.9 \text{ pixels} \sim 0.5 \text{ arcsec}$) and ($\text{FWHM} = 8.6 \text{ pixels} \sim 1 \text{ arcsec}$). As a second check, we also use the unresolved non-stellar continuum to determine the PSF. The FWHM of the Gaussians for the non-stellar continuum is, as expected, similar to what was determined with the broad Brackett emission: H band ($\text{FWHM} = 3.3 \text{ pixels} \sim 0.4 \text{ arcsec}$) and ($\text{FWHM} = 5.4 \text{ pixels} \sim 0.7 \text{ arcsec}$); K band ($\text{FWHM} = 3.9 \text{ pixels} \sim 0.5 \text{ arcsec}$) and ($\text{FWHM} = 8.7 \text{ pixels} \sim 1.1 \text{ arcsec}$).

The instrumental broadening is calculated by selecting and measuring the spectral broadening of an unblended sky emission line. The broadening varies as a function of wavelength and spatial position in our data cube; therefore, we select sky lines close to the wavelength of interest for our measurements. For the K band, we do this calculation for sky lines close to the wavelength of the [Si VI] 1.963 μm , $\text{Br}\gamma$ 2.166 μm , $1-0 \text{ S}(1) \text{ H}_2$ 2.1218 μm and [Ca VIII] 2.3211 μm emission lines for every spaxel in the sky emission cube. The instrumental broadening at the wavelength of each line is determined by doing a field-of-view spatial average of the best-fitting Gaussian σ . We obtain values which vary between $\sigma_{\text{inst}} \sim 42$ and 48 km s^{-1} in the K band. The spectral resolution at the wavelength of the $1-0 \text{ S}(1) \text{ H}_2$ emission is Half width at half maximum (HWHM) $\sim 3.3 \text{ \AA}$. For the H band, we obtain values of $\sigma_{\text{inst}} \sim 44$ – 54 km s^{-1} which at the wavelength of the [Fe II] 1.644 μm emission corresponds to HWHM $\sim 3.2 \text{ \AA}$ and a resolution of $R \sim 2500$.

As mentioned above, the broad hydrogen recombination lines of the Brackett series are present in both the H and K bands. In the H band, several of these lines overlap with stellar absorption lines of interest and therefore it was necessary to remove them before determining the stellar kinematics. The procedure was similar to the one described in Raimundo et al. (2013), where the broad emission lines were fitted simultaneously, while fixing their rest-frame wavelengths to a common redshift and relative intensities to the ones predicted theoretically using as an approximation Hummer & Storey (1987) for case B recombination. In the K band, only two broad emission lines were observed and they did not overlap with the wavelength range of the CO stellar absorption lines or the emission lines. For the K band, it was not necessary to remove the AGN broad hydrogen emission prior to the analysis of the stellar properties.

The flux calibration is done using the 2MASS measured fluxes in the H band and K_s band for a 5 arcsec diameter aperture. To determine the 2MASS fluxes, we use the zero-magnitude calibrations in Cohen, Wheaton & Megeath (2003). We then compare the 2MASS fluxes with the median number counts of the integrated spectra in our data cubes, for the same aperture. In our data cubes, the median number counts are determined within the waveband of [1.504–1.709] μm for the H band and [1.989–2.316] μm for the K band. These wavebands correspond to the wavelengths at which

the transmission in the 2MASS filters is higher than 0.2. By using different apertures in 2MASS, we determine that our calibration is consistent to ~ 20 per cent.

2.2 VIMOS data reduction

To investigate the emission in the optical wavelengths, we analysed archival Integral Field Unit (IFU) data of MCG–6–30–15 from 2004 using VIMOS/VLT. The data were taken with the old HR-blue grism (replaced by a new set of grisms in 2012) with a wavelength range 4200–6150 Å and a pixel scale of 0.67 arcsec pixel⁻¹ in a field of view of 27 arcsec × 27 arcsec. We reduced the data in each of the four quadrants using the ESO VIMOS pipeline and the standard recipes for doing the bias subtraction and flat-field correction, bad pixel removal, wavelength calibration and relative flux calibration with *vmbias*, *vmifucalib*, *vmifustandard* and *vmifuscience*. In quadrant three, we observed that there were zig-zagging patterns on its reconstructed image after *vmifuscience* which is caused by a fibre misidentification during *vmifucalib*. This has been observed in other data sets (e.g. Rodríguez-Zaurín et al. 2011). To solve this problem, we did not use a fibre identification file but ran the recipe with a ‘first guess’ fibre identification method; specifically, the arc lamp lines are identified using models of the spectral distortions as first guesses. Doing such a fibre identification improved the result but did not completely solve the problem. We then decided to change the maximum percentage of rejected positions in the fibre spectra tracing to a conservative value, i.e. when the fraction of rejected pixel positions was more than 17 per cent, the fibre was flagged as ‘dead’. As we only have one exposure for each quadrant, this results in some fibres being excluded (having no associated data) in the final data cube which is not ideal but preferable to having misidentified fibres. The final reconstructed image of the field of view and the final cube were obtained by combining the reduced data on the four quadrants using *vmifucombine* and *vmifucombinecube*, respectively. Final fibre-to-fibre transmission corrections were done using dedicated IDL routines and the fibre-to-fibre integrated flux in the sky line of [O I] $\lambda 5577$ Å. The same sky line was also used to verify the wavelength calibration and to determine the instrumental broadening which is $\sigma = 22$ km s⁻¹. The scope of our analysis is to determine the relative line intensity map and velocity profile for the [O III] emission and therefore no absolute flux corrections were done. Sky lines are observed in the spectra; however, as they are not confused with the object emission, they are not subtracted in the data cube.

Several emission lines are observed in the spectra: the strongest emission is [O III] 5007 Å but H β 4861 Å with a nuclear broad

component and a more spatially extended narrow component is also detected. Stellar absorption lines albeit with a lower signal-to-noise ratio (S/N) are also observed. The broad H β component originates from the AGN and is therefore unresolved in our data. We use its flux distribution to obtain an estimate for the PSF and the spatial resolution. Fitting the broad H β flux spatial distribution with a circular Gaussian, we find FWHM = 1.7 pixel which for our scale of 0.67 arcsec pixel⁻¹ corresponds to FWHM = 1.1 arcsec.

2.3 AGN and stellar continuum

The observed near-infrared (near-IR) continuum is a combination of stellar and non-stellar contributions. To evaluate the contribution of each of these components to the total continuum in the *H* band, we use the equivalent width of the CO (4–1) 1.578 μ m stellar absorption line, while in the *K* band we use the ¹²CO (3–1) 2.323 μ m line (Fig. 1). Close to the AGN, the stellar absorption line will be diluted and we expect the equivalent width to decrease as the distance from the AGN decreases. In the regions further away from the centre of the galaxy ($r \gtrsim 1.3$ arcsec), where the AGN contribution is negligible, the equivalent width will be due to stellar processes only and determines the intrinsic line equivalent width (W_{intr} ; Davies et al. 2007; Burtcher et al. 2015). The plots in Fig. 1 give us the observed equivalent width as a function of radius (W_{obs}). The fraction of the continuum which is due to non-stellar processes will then be

$$f_{\text{AGN}}(r) = 1 - \frac{W_{\text{obs}}(r)}{W_{\text{intr}}}, \quad (1)$$

and we can determine the AGN contribution to the continuum at each radial position. The total continuum at each position of the field of view is fitted using a second-degree polynomial. The AGN continuum is calculated by multiplying the total continuum by $f_{\text{AGN}}(r)$. The stellar continuum is determined from the depth of the stellar absorption lines present in our spectra. The continuum decomposition for the *H* and *K* bands is shown in Fig. 2. As expected, the non-stellar continuum is associated with the AGN and is limited to a small region close to the nucleus ($r \lesssim 0.5\text{--}0.8$ arcsec). The stellar continuum shows a more extended distribution.

3 RESULTS AND DISCUSSION

In the *H* band, after subtracting the broad hydrogen emission lines, various stellar absorption line features such as the CO absorption bands, Si I and Mg I are observed in the spectra. The only emission line observed, apart from the hydrogen recombination lines, is the

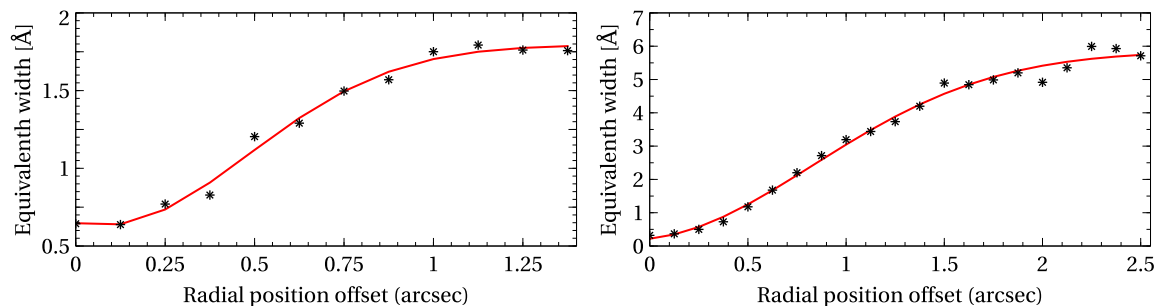


Figure 1. Left: equivalent width of the CO (4–1) 1.578 μ m line in the *H* band as a function of radius. Right: equivalent width of the ¹²CO (3–1) 2.3227 μ m line as a function of radius. The centre indicates the position of the black hole and is measured from the peak of the broad hydrogen Brackett emission. The equivalent widths are measured in annuli of 1 pixel (0.125 arcsec) width. The red lines in each of the plots are the best-fitting Gaussian curves to the data points. They are used in the subsequent decomposition of AGN and stellar continuum for the *H* and *K* bands.

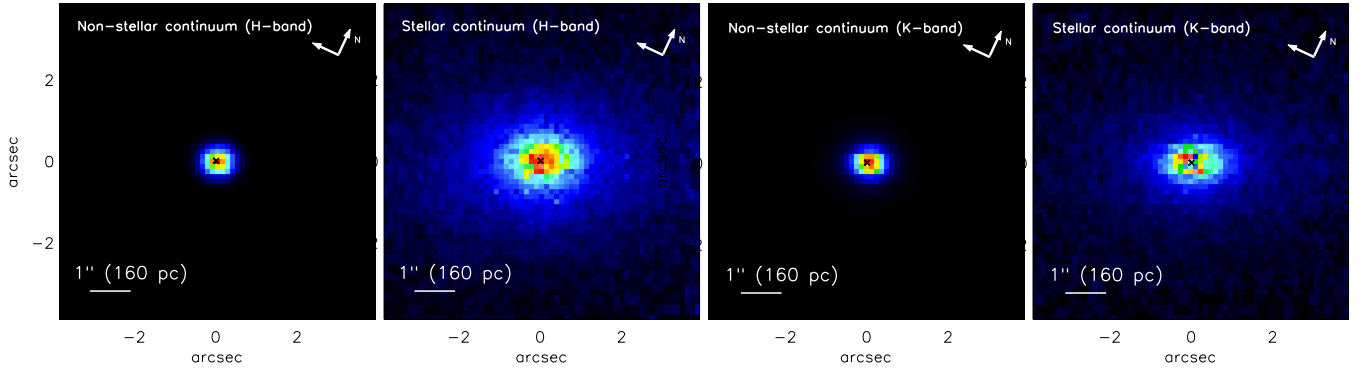


Figure 2. Non-stellar and stellar continuum maps after the continuum decomposition based on the stellar absorption lines’ equivalent widths. The two plots on the left show the H -band continuum and the two plots on the right show the K -band continuum. The position of the AGN is indicated by the black cross.

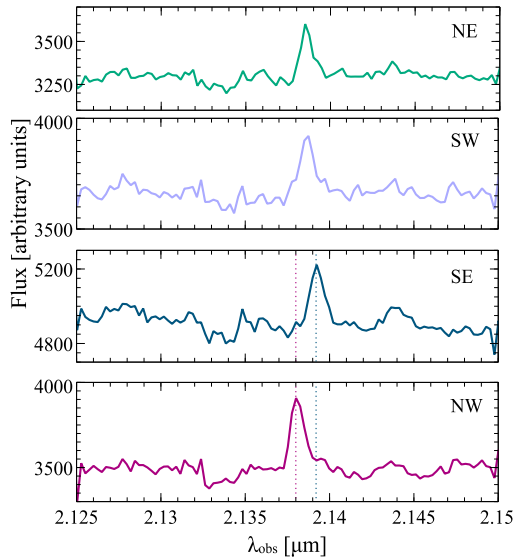


Figure 3. H_2 2.1218 μm emission from four regions of 5×5 pixels ($0.625 \text{ arcsec} \times 0.625 \text{ arcsec}$) in the field of view. From top to bottom: north-east, south-west, south-east and north-west from the nucleus. Relative to the images in Fig. 2, these regions are located at the left, right, top and bottom of the AGN position. The wavelength range in the plot shows the H_2 gas emission line. The emission at the SE and NW of the nucleus shows a clear redshift and blueshift. The vertical dashed lines indicate the position of the peak of the emission in each of these two regions. The x -axis is the observed wavelength.

[Fe II] 1.64 μm emission line. In the K band, we detect several stellar absorption features, including the CO absorption bands which are the strongest absorption lines in our spectra. The rovibrational H_2 2.12 μm emission is also detected and a tracer of the molecular gas distribution (Fig. 3). In addition, there are three other emission lines from ionized gas which are observed ([Si VI] 1.963 μm , Br γ 2.166 μm and [Ca VIII] 2.3211 μm) and will be analysed in the following sections. The nuclear spectrum of MCG–6-30-15 in the K band showing the Br γ and coronal emission lines can be seen in Fig. 4. H_2 is not significantly detected in the nuclear region.

3.1 Stellar kinematics

The stellar kinematics are obtained by fitting the observed galaxy spectra using the Penalized Pixel-Fitting (pPXF) method (van der Marel & Franx 1993; Cappellari & Emsellem 2004). The goal of this

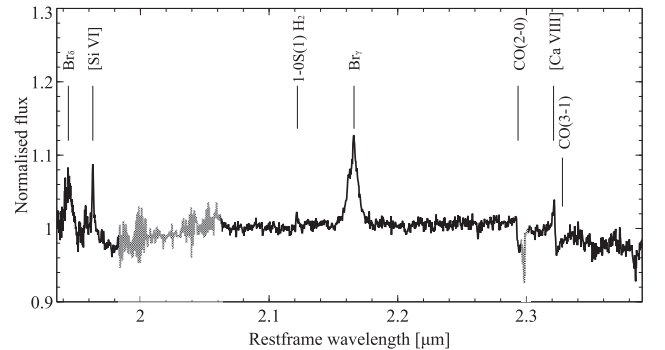


Figure 4. Spectrum of the nuclear region integrated in a 0.625 arcsec radius aperture. The inner $r < 0.25 \text{ arcsec}$ are excluded. The regions in grey indicate the presence of residuals from the telluric absorption correction.

method, and of our analysis, is to recover the line-of-sight velocity distribution from the stellar absorption features of our observed spectra. This method assumes a parametrization for the stellar line-of-sight velocity distribution on the form of a Gauss–Hermite series expansion, with the first two moments being the velocity and the velocity dispersion (V , σ). It then uses a set of stellar templates and a polynomial component to account for the AGN continuum, to find the best-weighted template combination and line-of-sight velocity distribution to fit the input galaxy spectra. Due to the limited S/N of our data, we only fit the first two moments of the velocity distribution.

In the H band, we use the stellar templates of Le et al. (2011) at a resolution of $R \sim 5000$. This library contains only 10 G, K and M giant stars, but as described in Raimundo et al. (2013), K and M stars provide a good match to our stellar absorption features. In the K band, we use the stellar templates from Winge, Riffel & Storchi-Bergmann (2009) in the near-IR wavelength range of 2.24–2.43 μm , at a resolution of $R = 5900$ obtained with GNIRS. We convolve these spectra with a Gaussian of $\sigma = 2.3 \text{ \AA}$ to match them to the lower resolution of our data.

The stellar kinematics from both the H and K bands are consistent with what was found in Raimundo et al. (2013). In Raimundo et al. (2013), we only had H -band data in a $3 \text{ arcsec} \times 3 \text{ arcsec}$ field of view, which allowed us to discover the counter-rotating core but not to study the main body of the galaxy extensively. With the larger field of view of our new H - and K -band observations ($8 \text{ arcsec} \times 8 \text{ arcsec}$), we are able to probe larger distances from the nucleus. Fig. 5 shows the fit to the integrated emission in the H and K bands. The black line shows the integrated galaxy spectrum and the red line

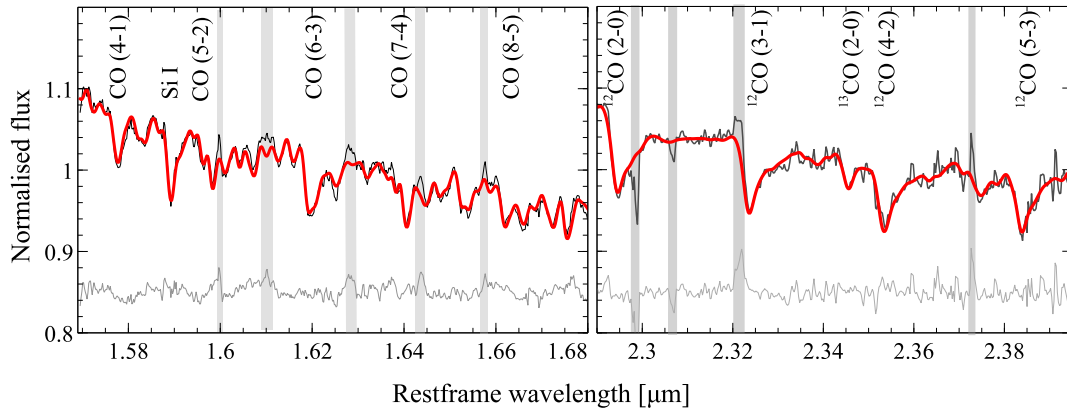


Figure 5. Data (black line), best-fitting model (red line) and residuals (bottom grey spectrum shifted by a constant factor to be visible in the plot) for the galactic spectrum fit with pPXF. Left: *H*-band integrated emission in an $r < 2$ arcsec region, excluding the inner $r < 0.5$ arcsec. Right: *K*-band integrated emission in an $r < 2.5$ arcsec region excluding the central $r < 0.25$ arcsec. The vertical shaded bands indicate the wavebands excluded from the fit. The x -axis is the rest-frame wavelength after correcting for the systemic velocity of the galaxy.

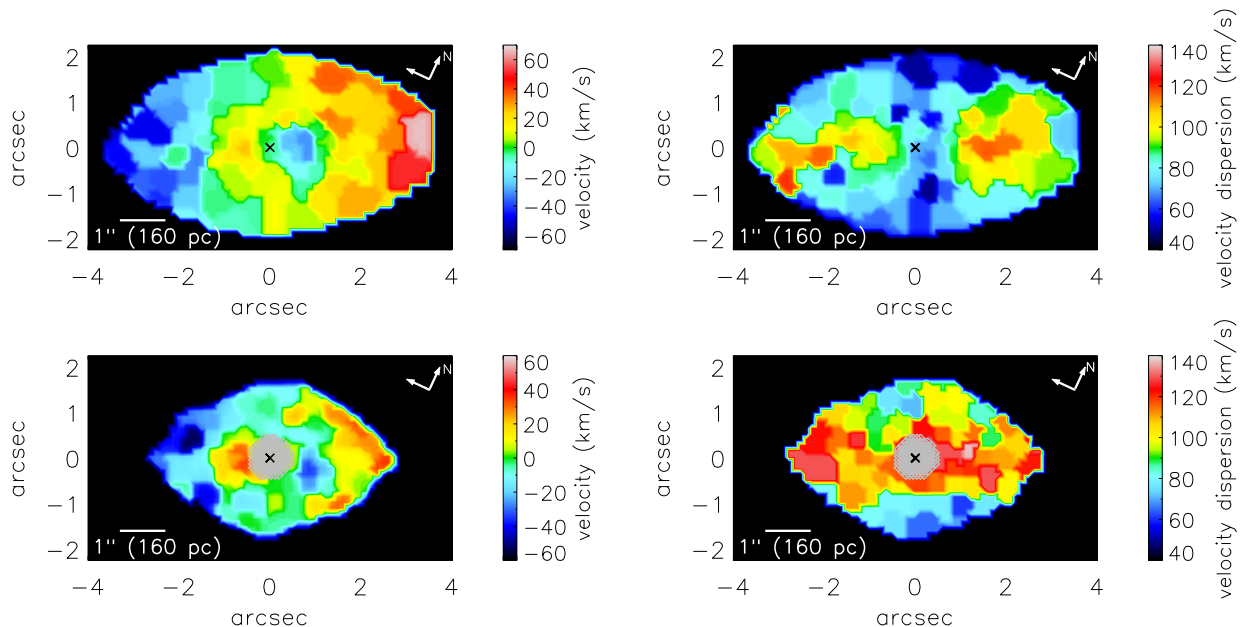


Figure 6. Stellar line-of-sight velocity and velocity dispersion maps for the *H* band (top) and *K* band (bottom). Left: line-of-sight velocity field corrected for the galaxy’s systemic velocity of 2410 km s^{-1} . Right: velocity dispersion corrected for the instrumental broadening. The map was binned to a minimum S/N of 5. The central regions were masked out due to the low S/N of the stellar absorption features and the outer regions were masked out due to a combination of low flux and low S/N.

shows the best-fitting model from pPXF. The residuals are shown in light grey at the bottom of the plot. Regions with emission lines and telluric subtraction residuals were masked out of the fit and are identified by the vertical shaded bars.

Each spatial pixel was then fitted using pPXF in a similar procedure to what was done for the integrated spectrum in Fig. 5. The maps were first binned to a minimum S/N ~ 5 between the depth of the CO stellar absorption lines and the noise in a line-free region of the spectra using the Voronoi binning technique described in Cappellari & Copin (2003). The stellar features in the *K* band are weaker and the map has to be more significantly binned to achieve the target S/N; furthermore, the inner regions show a high noise level due to the presence of the AGN emission, and therefore were masked out. The outer regions of both maps where the flux is low (less than 1 per cent of the peak flux) were also masked out. The maps of line-

of-sight velocity and velocity dispersion for the *H* and *K* bands are shown in Fig. 6. The KDC, characterized by a change in the rotation direction of the velocity field, is clearly observed in the centre of both the velocity field maps. Despite the lower S/N in the *K* band, the *K*-band velocity and velocity dispersion maps (Fig. 6, bottom panels) are consistent with the ones for the *H* band considering that the velocities measured in the *K* band have larger error bars (see below). Although for the final results we only fit for the first two moments of the velocity distribution, we tested a determination of the parameter $h3$, which is associated with asymmetric deviations from a Gaussian shape for the line-of-sight velocity distribution. The $h3$ map showed an anti-correlation with the velocity structure of the distinct core.

Using Monte Carlo simulations where the wavelength ranges for the fit and initial parameters are changed randomly, we estimate the

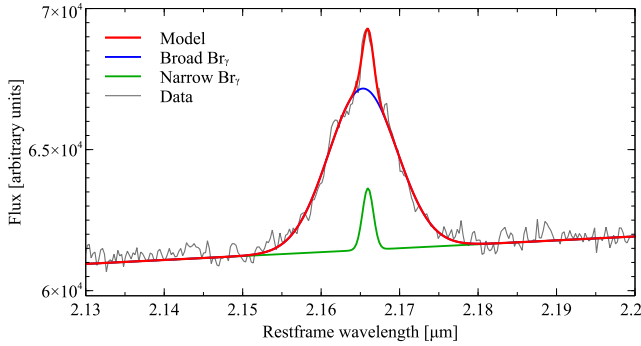


Figure 7. Fit to the hydrogen Brackett emission line in the K band which consists of two components: a broad one associated with the AGN and a narrow one which may have a contribution from star formation. The emission in the plot corresponds to an integrated region of 5×5 pixels ($0.625 \text{ arcsec} \times 0.625 \text{ arcsec}$) centred at the spatial position of the AGN. The x -axis is the rest-frame wavelength.

errors in the H -band velocity map to be typically 6 km s^{-1} except in the central regions close to the black hole where it reaches 13 km s^{-1} . The errors in the velocity dispersion are ~ 7 and 15 km s^{-1} in the centre. In the K -band map, we estimate the error in the velocity and velocity dispersion to be $< 10 \text{ km s}^{-1}$ out to $r < 2 \text{ arcsec}$. The outer regions ($r > 2 \text{ arcsec}$) and the central masked region have errors of $\sim 20\text{--}25 \text{ km s}^{-1}$ in both velocity and velocity dispersion.

The systemic velocity and position angle (PA) are determined using the method outlined in Krajnović et al. (2006). The kinematic PA for the distinct core is determined from the H -band velocity map limited to the region of $r < 1.1 \text{ arcsec}$. We find $\text{PA} = 118 \pm 22 \text{ deg}$ (3σ error) measured from north to east. The region outside the distinct core is modelled setting $r > 1.2$ and $r < 3.5 \text{ arcsec}$, and we find $\text{PA} = 112 \pm 8 \text{ deg}$ (3σ error). The similarity between these angles combined with the observation of the shift in the velocity field indicate that the distinct core is misaligned from the main body of the galaxy with an orientation consistent with counter-rotation (180 deg shift in the velocity orientation with respect to the main body of the galaxy).

3.2 Ionized gas

3.2.1 Hydrogen $\text{Br}\gamma$ emission

Broad hydrogen $\text{Br}\gamma$ $2.166 \mu\text{m}$ emission is detected in the region close to the AGN, and it is spatially unresolved by our data. The $\text{Br}\gamma$ emission also shows a narrow component which can be separated from the underlying broad component. Fig. 7 shows the integrated emission in a region of $0.625 \text{ arcsec} \times 0.625 \text{ arcsec}$ centred at the nucleus. This line shows a blueshift of $\sim 100\text{--}150 \text{ km s}^{-1}$ with respect to the systemic velocity of the galaxy, as found in Reynolds et al. (1997). The broad Brackett emission was used to determine the instrumental PSF and the centre of the PSF is taken as the spatial position of the AGN. Although the narrow emission may have a contribution from star formation, it is not detected significantly outside the PSF region. The velocity, dispersion and flux maps are shown in Fig. 8 (top row). Fig. 9 shows the stellar and gas emission velocity profiles along the major axis of the galaxy, averaged in a pseudo-slit of 3 pixel ($\sim 0.4 \text{ arcsec}$) width. The kinematics of $\text{Br}\gamma$ resemble a rotation pattern and is very similar to the one of the stars in terms of the velocity gradient and low dispersion.

The $\text{Br}\gamma$ narrow-line flux can be used to estimate the star formation rate or to determine upper limits for it in galaxies where

stars provide the only excitation mechanism for $\text{Br}\gamma$ (e.g. Panuzzo et al. 2003; Valencia et al. 2012; Smajić et al. 2014). In the case of MCG–6–30–15, the spatial distribution of $\text{Br}\gamma$ when compared with the stellar distribution profile leads us to believe that this emission is mainly associated with the AGN, although some smaller contribution from star formation is also possible. As noted by Smajić et al. (2014), assuming that all of the central $\text{Br}\gamma$ emission is due to star formation is an unlikely scenario for a Seyfert galaxy. We can however use the equivalent width of the narrow $\text{Br}\gamma$ line to set upper limits on the star formation. In the integrated central region of $0.625 \text{ arcsec} \times 0.625 \text{ arcsec}$, the width of the narrow line is $\sim 15 \text{ \AA}$. This is a low value (similar values have been found for other Seyfert galaxies; Davies et al. 2007), which indicates that there is little star formation ongoing in this galaxy. If star formation is occurring, it is possibly in the form of short bursts, in line with what is observed in the ultraviolet spectra (Bonatto et al. 2000).

3.2.2 $[\text{Fe II}]$ emission

The forbidden $[\text{Fe II}]$ emission line at $1.644 \mu\text{m}$ was first detected in the H -band observations in Raimundo et al. (2013), extending out to a radius of $r < 0.8 \text{ arcsec}$. With the new data in the present work covering a wider field of view and at a higher S/N, we were able to study the distribution of ionized gas further out in the galaxy (Fig. 8, second row). For the analysis of the ionized gas emission, we use the code LINEFIT (appendix B of Davies et al. 2011) to fit the emission line at each spatial position of our field of view. LINEFIT uses a sky emission line observed close to the wavelength of interest as a template for the emission, and then convolves it with a Gaussian kernel to match the observed line profile. The instrumental broadening is therefore automatically accounted for when fitting the lines. Individual pixels with $\text{S/N} < 3$ (between the peak of the line and the rms noise of the continuum) were masked out of the image. We observe that the $[\text{Fe II}]$ line flux does not peak at the position of the nucleus but at a position north-west of the nucleus, as in the first time it was detected (Raimundo et al. 2013). The velocity map indicates an overall bulk rotational velocity direction similar to the one of the stellar counter-rotating core, albeit with a higher rotational velocity $[-70, 60] \text{ km s}^{-1}$. We can now distinguish further structure in the velocity dispersion map. The forbidden transition of $[\text{Fe II}]$ is excited by electron collisions. To achieve the right conditions for this line emission, it is necessary to have a zone of partially ionized hydrogen where Fe^+ and e^- coexist. In AGN in particular, $[\text{Fe II}]$ emission can be generated by photoionization by the central AGN or by shocks (caused by the interaction of radio jets with the medium, by nuclear mass outflow shocks with ambient clouds or by supernova-driven shocks; Mouri, Kawara & Taniguchi 2000; Rodríguez-Ardila et al. 2004). Correlations have been found between the radio properties of Seyferts and the presence of $[\text{Fe II}]$ (Forbes & Ward 1993; Ramos Almeida et al. 2006; Riffel, Storchi-Bergmann & Nagar 2010) which indicates that shocks associated with radio jets may be the main excitation mechanism in some active galaxies. Mundell et al. (2009) analysis of radio data on MCG–6–30–15 find a possible elongation in the extended radio emission approximately perpendicular to the orientation of the $[\text{O III}]$ emission which may indicate the presence of a jet-like or disc wind component. However, the $[\text{Fe II}]$ emission has a similar orientation to the $[\text{O III}]$ emission and therefore it is unlikely that shocks associated with a possible radio jet are the main excitation mechanism for $[\text{Fe II}]$ emission in this galaxy.

In our previous work (Raimundo et al. 2013), we hypothesized that the $[\text{Fe II}]$ emission was caused mainly by supernova shocks

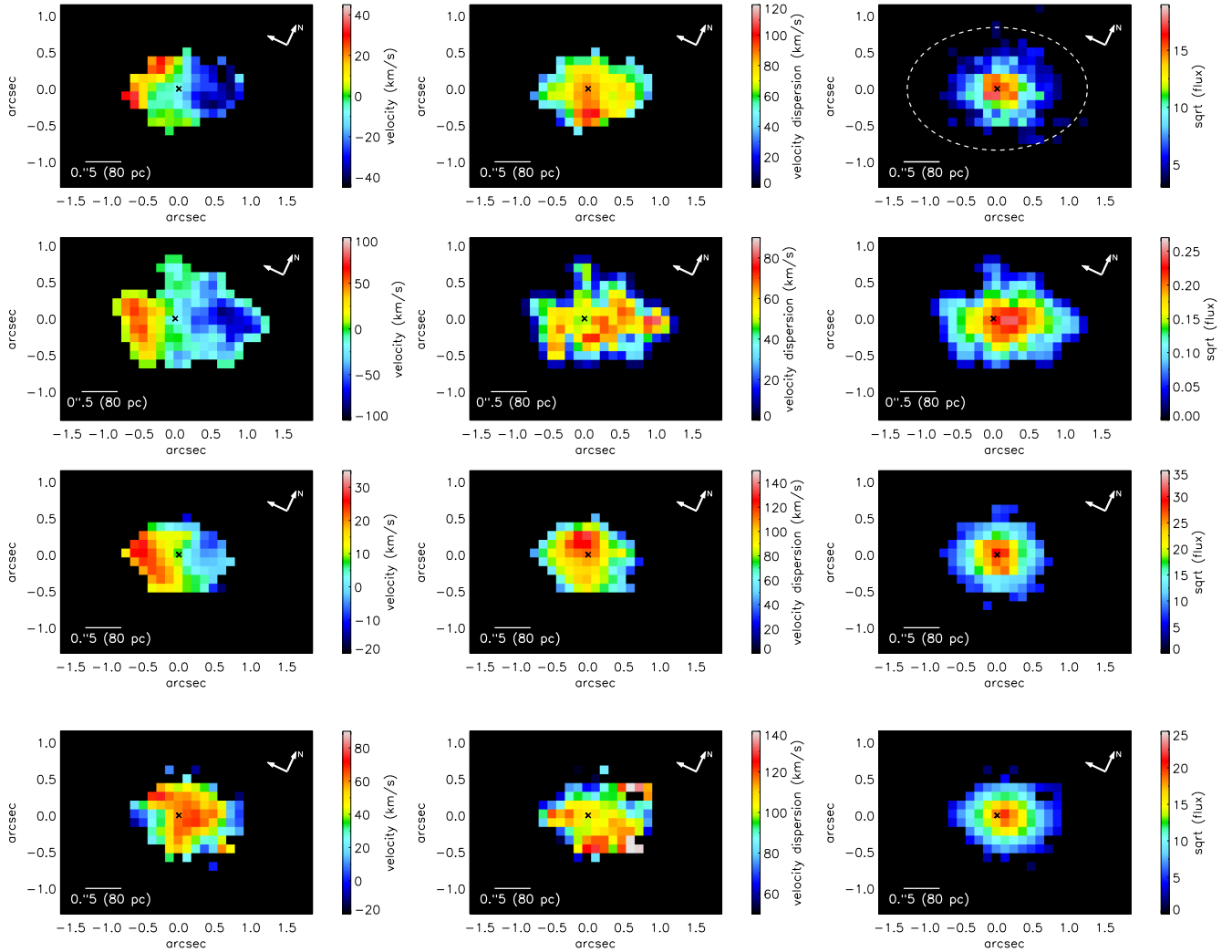


Figure 8. Velocity, velocity dispersion and flux maps of the ionized gas emission lines in our spectra. Top to bottom: narrow $\text{Br}\gamma$, $[\text{Fe II}]$, $[\text{Si VI}]$ and $[\text{Ca VIII}]$. The velocities were corrected for the systemic velocity of the galaxy and instrumental broadening. Minimum S/N is 3.0. The cross indicates the AGN position. The white ellipse in the top panel indicates the size of the stellar KDC.

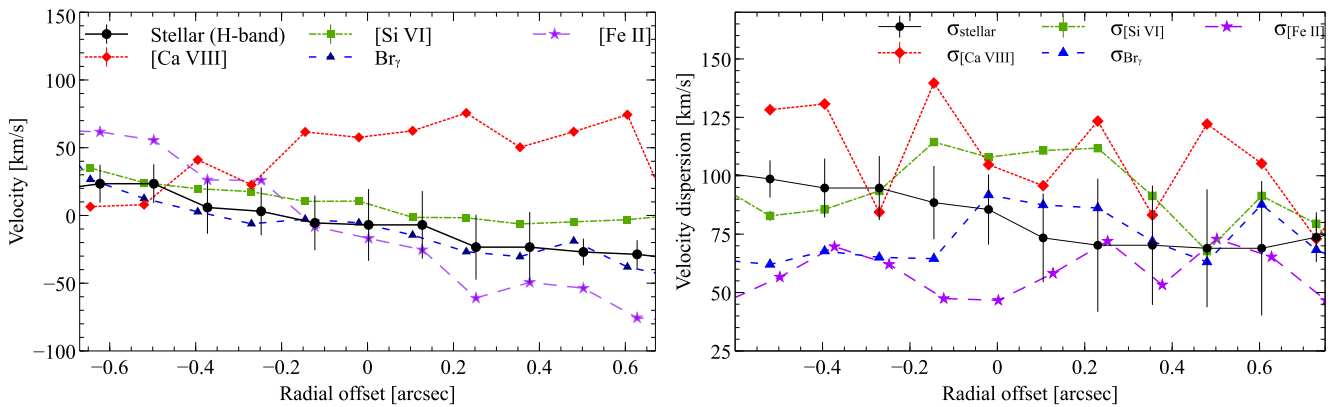


Figure 9. Horizontal cuts along the major axis of the galaxy to measure the ionized gas and the H -band measured stellar dynamics as a function of radius from the AGN position. Left: velocity. Right: velocity dispersion.

from a previous star formation event and our new observations support this scenario. The spatial distribution of the $[\text{Fe II}]$ coincides with the region where we see the strongest S/N in the stellar absorption features and although we detect an AGN-driven outflow

in our data, the dynamics of $[\text{Fe II}]$ resembles a rotation pattern and is distinct from the $[\text{Ca VIII}]$ dynamics (Fig. 9). The following additional indications are present in the data. First, we observe that the $[\text{Fe II}]$ emission extends further out than the $[\text{Si VI}]$ and $\text{Br}\gamma$

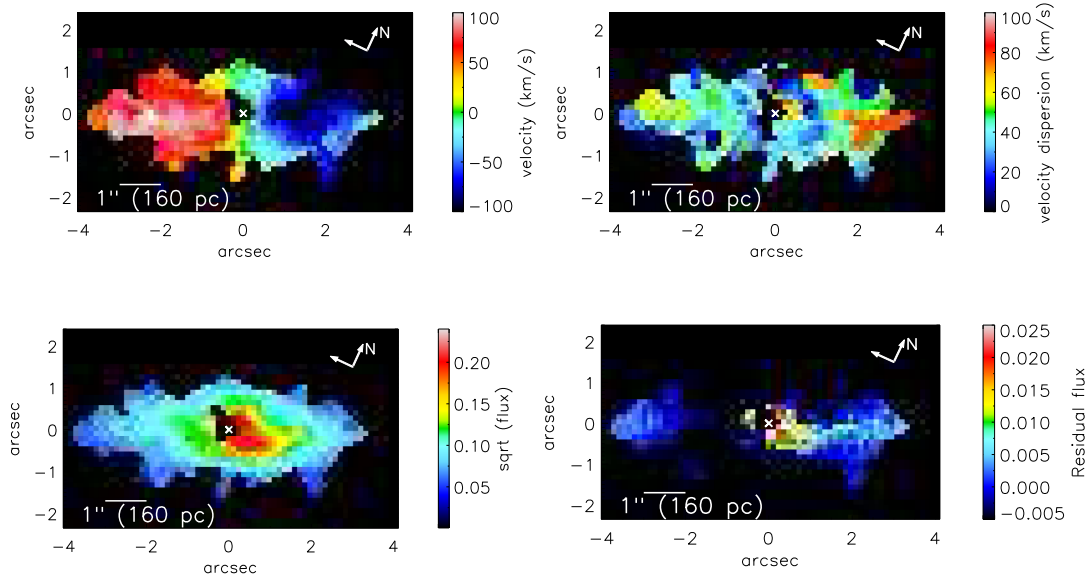


Figure 10. H_2 2.12 μm distribution and dynamics. Top left: velocity map. Top right: velocity dispersion. Bottom left: flux map. Bottom right: flux residuals after subtracting elliptical isophotes. The H_2 rotation direction is the same as for the counter-rotating core. The spatial extent of the H_2 is larger than the counter-rotating core. The map was binned to a minimum S/N of 5. In the central regions, the H_2 emission is not detected at a significant S/N level; therefore, these central pixels were masked out of the image.

emission (Fig. 8). Secondly, the $[\text{Fe II}]$ emission is not centred at the nucleus and seems to trace a similar distribution to what is seen for the molecular gas (traced by the H_2 emission in Fig. 10), which would be expected if both these lines originate from regions of star formation. Thirdly, the velocity dispersion map shows peaks in various regions of the $[\text{Fe II}]$ emission which could be tracing the local dynamics and be associated with locations of major supernova events. The general $[\text{Fe II}]$ velocity dispersion profile along the major axis, as can be seen in the right-hand panel of Fig. 9, is lower than for the stars or the other ionized species, but closer to the dispersion profile of H_2 , further indicating that these two lines may be tracing the same regions of star formation and supernova events. It would be expected that if $[\text{Fe II}]$ and H_2 are being excited in the same regions, the ionized gas traced by $[\text{Fe II}]$ would show more disturbed kinematics (higher velocity dispersion) than the molecular gas traced by H_2 .

It is of course likely that AGN photoionization also contributes to the $[\text{Fe II}]$ emission, even if it is not the dominant mechanism (Rodríguez-Ardila et al. 2004). The $[\text{Fe II}]$ emission will then provide an upper limit for the number of supernova events. With our new observations, we can probe the $[\text{Fe II}]$ emission within the full extent of the KDC and improve the $[\text{Fe II}]$ flux measurement in Raimundo et al. (2013). Integrating for the regions with emission S/N > 3, we obtain $F_{[\text{Fe II}]} = 3.0 \times 10^{-15} \text{ erg s}^{-1} \text{ cm}^{-2}$ and $L_{[\text{Fe II}]} = 4 \times 10^{38} \text{ erg s}^{-1}$.

3.2.3 Coronal line emission

Two high-ionization coronal lines are detected in the K-band observations: $[\text{Si VI}]$ 1.963 μm and $[\text{Ca VIII}]$ 2.321 μm . These lines are a good tracer of AGN activity due to their high ionization potential (IP > 100 eV). $[\text{Si VI}]$ (IP = 167 eV) is mainly detected in the nucleus with a spatial extent of the order of the instrumental PSF. The velocity and velocity dispersion maps with a minimum S/N ~ 3 are presented in Fig. 8 (third row). The regions with flux less than 5 per cent of that of the peak were masked out of the maps. $[\text{Ca VIII}]$

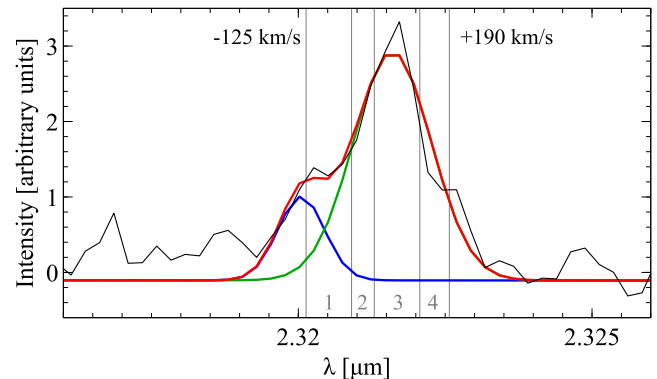


Figure 11. $[\text{Ca VIII}]$ emission integrated in a 1 arcsec \times 1 arcsec region centred at the nucleus as a function of rest-frame wavelength. The figure shows the observed spectrum in black, the total line fit (red line) and the two Gaussian components of the fit (blue and green). The vertical lines indicate the velocity bins used for the tomography analysis (-125 , -25 , $+25$, $+125$ and $+190 \text{ km s}^{-1}$). The numbers 1 to 4 indicate the corresponding panels of Fig. 12.

has a lower ionization potential (IP = 127 eV), and it is observed at a higher S/N than $[\text{Si VI}]$. Its emission is compact but resolved, slightly more extended than $[\text{Si VI}]$ and asymmetric with its flux emission peak north-west of the nucleus. The shape of the $[\text{Ca VIII}]$ emission line is complex, as can be seen in Fig. 11. This plot shows the line profile integrated in a 1 arcsec \times 1 arcsec region centred at the nucleus. The emission line can be fitted using two Gaussians, and that holds true for most of the pixels in the map with observed emission. The two lines are blueshifted and redshifted with respect to the systemic velocity of the galaxy and observed simultaneously at each spatial position, which is an indication that we are seeing the approaching and receding sides of a single ionization cone. To better understand the properties of this emission, we measured the flux at various velocity bins (‘velocity tomography’) and plot the result in Fig. 12. We can see that the $[\text{Ca VIII}]$ dynamics is dominated by an

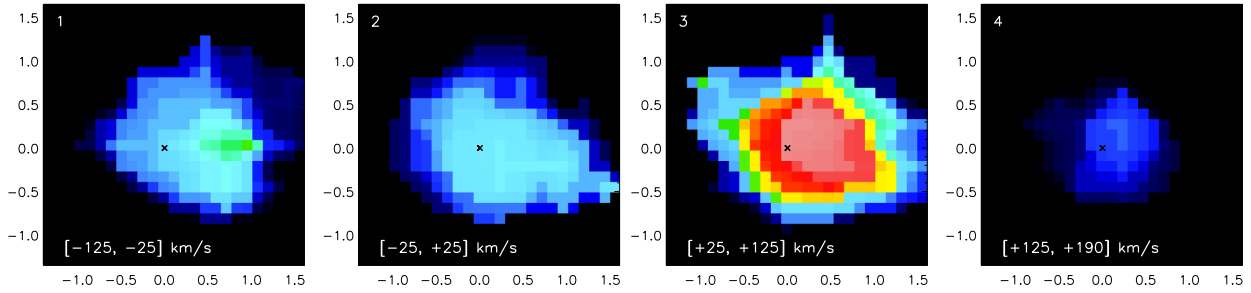


Figure 12. Velocity tomography of the [Ca VIII] line. Velocity intervals indicated at the bottom correspond to deviations from the systemic velocity of the galaxy and correspond to the regions (1 to 4) delimited by the vertical lines in Fig. 11. The spatial scale is arcsec and the orientation is the same as in Fig. 8. The first and third panels show the blueshifted and redshifted components of the outflow, respectively. This suggests that we are seeing the approaching and receding sides of a one-sided ionization cone.

Table 1. The radial extent is measured in radius from the nucleus.

Emission line	Spatial extent of the coronal line emission region	
	IP	Extent (radial)
[Si VI] 1.963 μm	167 eV	0.7 arcsec (~ 110 pc)
[Ca VIII] 2.321 μm	127 eV	0.9 arcsec (~ 140 pc)

outflow. The first plot on the left maps the blueshifted component of the outflow at up to -125 km s^{-1} . The nuclear component is seen in the second plot from the left and the strong redshifted component is seen in the third plot from the left, with velocities up to 125 km s^{-1} . In Fig. 8, we show the results of fitting the [Ca VIII] emission with a single Gaussian line. Although the shape of the real emission is more complex, these maps reflect the dynamics of the dominating redshifted component outflowing at velocities $\sim 100 \text{ km s}^{-1}$.

The [Si VI] emission could also have a redshifted outflowing component, as the velocities north-west of the nucleus are slightly higher than expected based solely on rotation and the dispersion is higher than that observed in the narrow Br γ emission (Fig. 9). However, due to its higher ionizing potential, this outflowing component is not as strong as in [Ca VIII]. The velocity tomography for [Si VI] shows a very centrally concentrated emission, which does not extend beyond the PSF. The extent of the coronal line region for both these lines is shown in Table 1. We define the extent of the coronal line region at the position where the flux of the line drops to 5 per cent of its peak value.

When comparing the profiles of the ionized gas emission with the one of the stars, we see clearly that narrow Br γ has a profile similar to the stars. [Si VI] and [Ca VIII] show a redshift in relation to the stellar rotation. The redshift of the [Si VI] is small and it is close to the range of errors expected for the stellar velocity. [Ca VIII] has a clearly distinct velocity profile, dominated by the redshifted component of the outflow. Although also slightly distinct from the stellar, the Br γ and the [Si VI] profiles, the velocity gradient of [Fe II] is clearly different from [Ca VIII] which is another indication that the [Fe II] emission is not part of the AGN outflow but tracing star formation in the disc. The study of Rodríguez-Ardila et al. (2006) on the size of the coronal line region in MCG-6-30-15 shows that the [Fe VII] line with an ionization potential of IP = 100 eV close to the one of [Ca VIII] (IP = 127 eV) shows an extent of $\lesssim 140$ pc (after converting to our cosmological parameters) similar to the spatial extent we observe in our study (Table 1). Rodríguez-Ardila et al. (2006) also find that the broad component of [Fe VII] is blueshifted and has a FWHM $\sim 670 \text{ km s}^{-1}$, which has been interpreted as signature of an outflowing wind. Blueshifted outflows have also been detected

in MCG-6-30-15 from X-ray studies of warm absorbers (Sako et al. 2003; Blustin et al. 2005; Chiang & Fabian 2011). These outflows present blueshifted velocities of $v_{\text{out}} = -1900$ and -150 km s^{-1} at distances of 0.036 and 5.7 pc from the nucleus, respectively, although it is not clear if the two outflows are part of the same accelerating wind (Blustin et al. 2005). The outflows at small scales may be associated with the [Ca VIII] outflow at scales of $r < 140$ pc which we observe in this work; however, it is difficult to establish a direct connection between such a large range of physical scales. Assuming that the faster outflow at $r \sim 0.036$ pc would lose velocity as it propagates, its velocity would have to decrease as $v_{\text{out}} \propto r^{-0.4}$ to reproduce the outflow we observe in [Ca VIII] at $r \sim 140$ pc.

3.2.4 Optical emission lines

In the VIMOS data cube, we detect two strong emission lines: [O III] 5007 and H β 4861 \AA (with a nuclear broad component and a spatially extended narrow component). To study the gas dynamics, we first use the stellar absorption lines to determine the galaxy's systemic velocity. We integrate the data cube spatially in the region of the field of view with highest contribution from the galaxy to determine an integrated spectrum. We then use pPXF and a set of stellar optical templates (Vazdekis 1999) to determine the systemic velocity. This velocity is then used as a reference for the study of the gas dynamics. To analyse the H β narrow component, we subtract the broad H β component from the spectra. As noted previously by Reynolds et al. (1997), the broad H β line can be fitted by two components, with the strongest flux being in a component blueshifted by $\sim 150\text{--}200 \text{ km s}^{-1}$ with respect to the systemic velocity of the galaxy. In Fig. 13, we show the line emission maps for the [O III] and the narrow H β . Pixels with S/N < 5 between the peak of the line and the noise in a line-free region of the continuum were masked out. The H β emission extends out to $r \sim 400$ pc, significantly more extended than the coronal lines detected in the near-IR. Its velocity map shows a rotation pattern counter-rotating with respect to the main body of the galaxy.

The [O III] emission is the most extended gas emission we detect. The line is detected out to $r < 10$ arcsec ~ 1.5 kpc above a S/N of 5. The dynamics in the region to the south-east of the nucleus match what we observe in the molecular gas (in terms of the rotational velocity expected and counter-rotation). To the north-west of the nucleus, the velocity dispersion increases and the velocity does not match the rotational pattern. We are likely observing the large-scale counterpart of the gas outflow observed in [Ca VIII]. In this region to the north-west of the nucleus, we observe velocities of

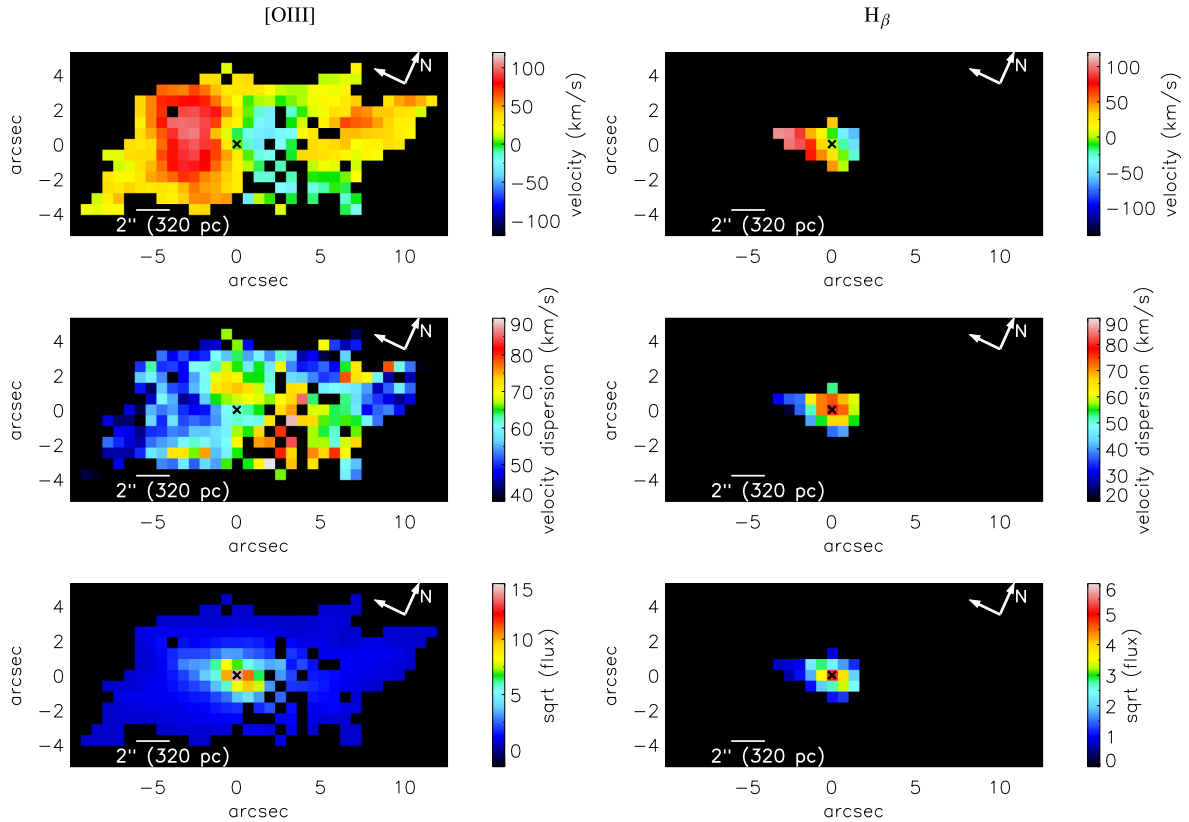


Figure 13. Ionized gas optical line emission maps. Left column shows the [O III] line emission maps and the right column shows the narrow H β emission. Top row: velocity maps. Centre: dispersion maps corrected for instrumental broadening. Bottom: flux maps.

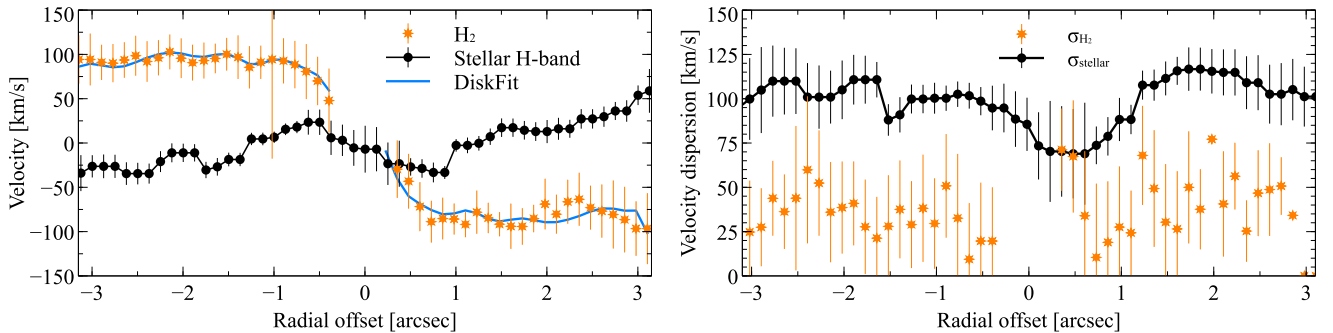


Figure 14. Horizontal cuts along PA = 122.5 deg for the molecular gas emission. The x-axis indicates the radial distance from the AGN position. Left: velocity. Right: velocity dispersion. The orange stars represent the H $_2$ properties while the blue solid line is the best-fitting velocity from the DISKFIT routine.

50–60 km s $^{-1}$ at $r \sim 1$ kpc which roughly matches the decrease in velocity expected if $v_{\text{out}} \propto r^{-0.4}$.

3.3 Molecular gas

The molecular gas is traced by the 1–0 S(1) H $_2$ distribution at 2.1218 μm which extends further out than the KDC. However, the direction of rotation for the gas is the same as for the distinct core – the molecular gas is also counter-rotating with respect to the main body of the galaxy, as can be seen in Fig. 10. The emission line map was binned to a S/N of 5 and the pixels with S/N lower than 3 were masked out of the map. The regions with low line flux, less than 5 per cent of the peak value, were also masked out. The velocity dispersion of the gas is low, typically ~ 25 –50 km s $^{-1}$. The molecular gas distribution is more disc-like than the stellar distri-

bution; the axial ratio is ~ 0.5 in comparison with the axial ratio of ~ 0.6 from the stellar continuum. The H $_2$ rotational velocity is significantly higher than the H $_2$ velocity dispersion, which indicates that the gas is rotationally supported. A comparison between the velocity and velocity dispersion of the molecular gas and stars along the major axis of the galaxy is shown in Fig. 14. We use the method of Krajnović et al. (2006) to determine the kinematic PA. Excluding the central $r < 0.5$ arcsec, we find PA = 122.5 \pm 3.5 deg. The PA of the gas is marginally consistent with both the distinct core and the outer regions of the galaxy, indicating that the molecular gas shares the same orientation as the stars, i.e. counter-rotating with respect to the main body of the galaxy. As can be seen in Fig. 10, the flux distribution for H $_2$ does not peak at the nucleus but in a region south-west of the nucleus. To better explore this asymmetry, we fit elliptical isophotes to the H $_2$ flux map centred at the AGN

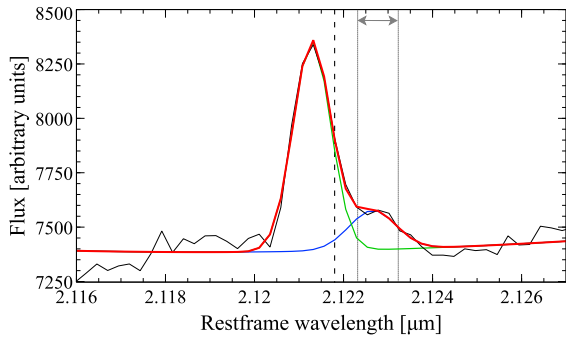


Figure 15. Emission line profile of H_2 at the peak in line flux, 0.8 arcsec SW of the nucleus, integrated in a $0.7 \text{ arcsec} \times 0.7 \text{ arcsec}$ region. The vertical dashed line indicates the line wavelength corresponding to the systemic velocity of the galaxy. The vertical dotted lines limit the region used in the analysis in Fig. 16.

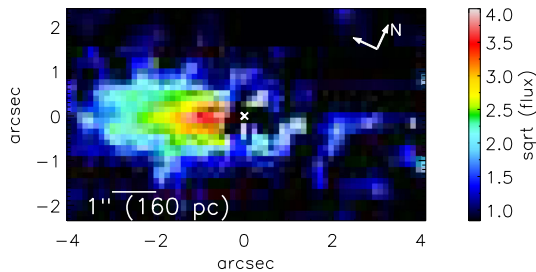


Figure 16. Flux map of the H_2 line emission between velocities $+70$ and $+200 \text{ km s}^{-1}$ (indicated by the vertical dotted lines in Fig. 15). In addition to the expected disc rotation component south-east of the nucleus, a weaker component is observed south-west of the nucleus and extending towards the west, apparently matching the distribution of flux residuals in the bottom-right panel of Fig. 10.

position and having the same PA and ellipticity as the large-scale H_2 distribution. In the bottom-right plot of Fig. 10, we show the flux residuals after removing these elliptical isophotes from the original H_2 flux map. In this figure, it is possible to see more clearly that there is a strong H_2 emission component 0.8 arcsec SW of the nucleus which extends to the west at least out to 2 arcsec. In this region of higher flux, we also observe a second weaker component in the line emission spectrum, redshifted from what is expected from the rotation pattern. In Fig. 15, we show the line profile integrated in a $0.7 \text{ arcsec} \times 0.7 \text{ arcsec}$ region 0.8 arcsec SW of the nucleus showing these two line components. The velocity of the gas in the redshifted component is $\sim +120 \text{ km s}^{-1}$ in a region where the H_2 disc shows a velocity of -75 km s^{-1} . The velocity dispersion is $\sigma \sim 57 \text{ km s}^{-1}$ which is slightly but not significantly higher than what we observe in the bulk disc component. In Fig. 16, we show a map of the flux integrated within the waveband where we observe the redshifted ‘bump’ component in the H_2 line emission. This waveband corresponds to velocities between $[+70, +200] \text{ km s}^{-1}$ indicated by the vertical dotted lines in Fig. 15. The map has been smoothed using a 3×3 boxcar median. When trying to identify the redshifted component at $V \sim 120 \text{ km s}^{-1}$, we are also sensitive to the disc rotation redshifted component to the south-east of the nucleus. In the region where the disc emission is blueshifted ($v_{\text{rot}} \sim -50 \text{ km s}^{-1}$), we can detect the red bump at velocities $\sim +120 \text{ km s}^{-1}$. However, it is not clear if this red ‘bump’ is present to the south-east of the nucleus as the main disc component there is expected to have velocities be-

tween 50 and 100 km s^{-1} . In Fig. 16, we can identify two regions: to the south-east of the nucleus we observe the expected redshifted component of the H_2 disc rotation; to the south-west flux residuals within the velocity interval $[+70, +200] \text{ km s}^{-1}$ are observed, which illustrates the regions where the red ‘bump’ emission is observed. Along the filamentary structure which extends to the west out to ~ 2 arcsec, we also observe that the H_2 line shows an asymmetric shape with an extended red wing, which can also be seen as emission in the map of Fig. 16. However, the S/N in this region is lower and we cannot obtain robust measurements of the velocity or velocity dispersion of the redshifted component here. The H_2 velocity map is modelled using the code DISKFIT version 1.2 (Spekkens & Sellwood 2007; Sellwood & Sánchez 2010; Sellwood & Spekkens 2015). We apply DISKFIT to our H_2 velocity field to fit the circular speed of the gas at each radius. The code minimizes the χ^2 difference between a model convolved with the PSF of the observations and the input data, which in our case is the 2D velocity field derived from the H_2 line fit. The code also takes into account the uncertainties in the velocity measurements. The input error map is obtained by doing Monte Carlo simulations on our line fit considering the typical noise observed in the spectra and varying the initial parameters for the fit. We fit a simple axisymmetric disc rotation model to the data, with the inclination, position of the centre, systemic velocity and PA as free parameters. The data, best-fitting model and residuals are shown in Fig. 17. The systemic velocity used is the one calculated by DISKFIT ($V_{\text{sys}} = 2392 \pm 1 \text{ km s}^{-1}$), which is lower by $\sim 18 \text{ km s}^{-1}$ in relation to the systemic velocity determined from the stellar velocity field. The velocity field is well reproduced by a rotating disc with a $\text{PA} = 122.4 \pm 1 \text{ deg}$ consistent with what was found with the method of Krajnović et al. (2006), ellipticity of $(1 - b/a) = 0.51 \pm 0.03$ and a disc inclination of $i = 60.9 \pm 1.9 \text{ deg}$. The errors were obtained using a bootstrapping method. The velocity residuals have values lower than 25 km s^{-1} in general which shows that the H_2 dynamics can be relatively well represented by rotation in a disc. There are no significant trends in the velocity residuals which may indicate that due to its lower flux, the redshifted component observed in the SW region does not affect significantly the velocity measurements. The largest velocity residuals from DISKFIT are observed ~ 3 arcsec south-west of the nucleus in a region which coincides with the residuals in flux after subtracting isophotes and also with a region of higher velocity dispersion. The flux and velocity residual and the higher velocity dispersion in this region could be caused by an outflow superimposed on rotation or by gas flow in the disc departing from circular rotation as observed in NGC 3227 (Davies et al. 2014). In Fig. 18, we compare the spatial distribution of the H_2 flux with the position of the dust lane just south of the nucleus. We use the *Hubble Space Telescope* (*HST*) archival image of MCG-6-30-15 taken in the WFC3/UVIS1 medium-band filter *f547M* with peak wavelength at 5475 \AA . The two panels on the left show the flux contours and the two panels on the right show the flux residual contours (after subtracting elliptical isophotes) superimposed on the *HST* image. The H_2 emission seems to originate from a large-scale region which includes the dust lane. The contours of the flux residuals seem to indicate that this flux component is coming from the dust lane. This can be an explanation for the redshifted H_2 component we observe in this region which also appears in the region of the flux residuals as can be seen in Fig. 16. We are likely in the presence of two components, one from a rotating disc close to the AGN and another originating in the dust lane and therefore presenting a different velocity. If the dust lane is between us and the centre of the galaxy, with our line of sight to the nucleus passing just above the dust lane (as it seems to be based on

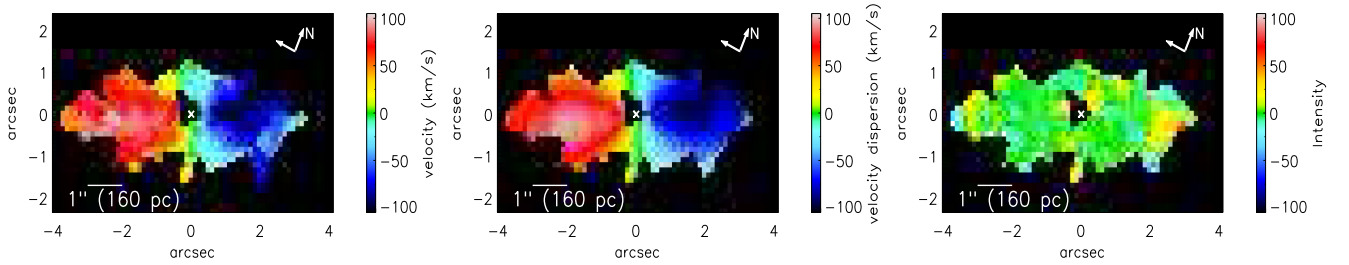


Figure 17. Velocity field, best-fitting Keplerian disc model from `DISKFIT` and velocity residuals for the H_2 emission. The maps were smoothed using a 3×3 pixel median.

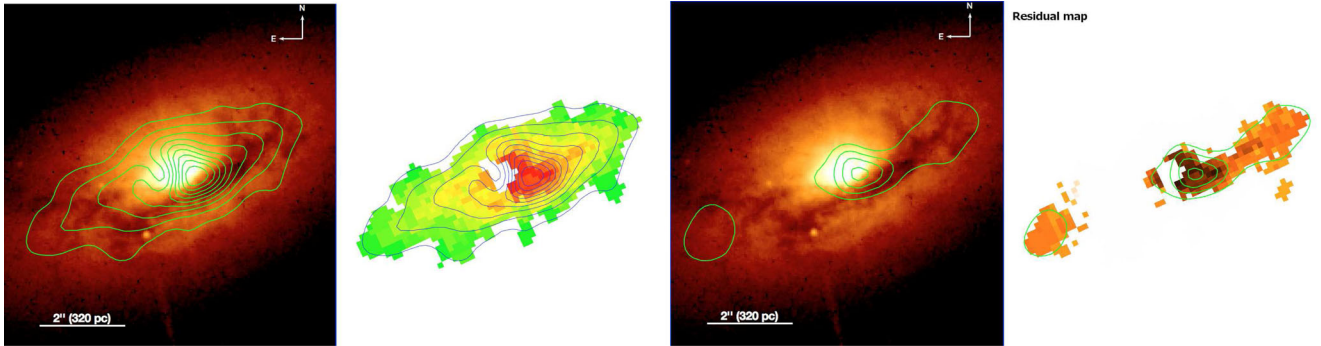


Figure 18. H_2 flux contours overlaid in the *HST* WFC3/UVIS1 $f547M$ archival image of MCG–6–30–15. Left pair of panels: flux contours. Right pair of panels: flux residual contours.

the obscuration of the optical light and from the X-ray study of the warm absorber in this galaxy; Ballantyne, Weingartner & Murray 2003), we would expect to observe a blueshifted H_2 component with respect to the systemic velocity of the galaxy. The fact that we observe a redshifted velocity indicates that the gas in the dust lane is moving towards the centre of the galaxy. Although the H_2 flux residuals appear to be spatially coincident with the dust lane, this may be a coincidence. If molecular clouds in the disc of the galaxy are being excited by ultraviolet fluorescence from the AGN, then the redshifted ‘bump’ could be associated with the receding side of the ionization cone which is associated with the $[\text{Ca VII}]$ emission as well. Unfortunately, the S/N in the H_2 line does not allow us to rule out one of these scenarios. Better S/N observations of H_2 could trace the presence (or absence) of emission in the dust lane to the south-east of the nucleus. High-resolution observations in the submillimetre could also trace colder molecular gas and determine if its distribution matches the dust lane.

3.3.1 Molecular gas excitation and molecular gas mass

The main processes responsible for H_2 emission are collisions with warm gas ($T \sim 2000$ K) which has been heated by shocks, either from supernova- or AGN-driven outflows, or X-ray irradiation (i.e. thermal processes), or by UV fluorescence, where excitation by a UV photon produces a radiative cascade through various rotational and vibrational states of H_2 (i.e. non-thermal processes; e.g. Mazzalay et al. 2013). Each of these mechanisms will produce a different emission spectrum and in theory it is possible to determine which one dominates. The only other transition of H_2 we detect is 1–0 S(3) 1.9576 μm . Its spatial distribution follows the one of 1–0 S(1) but at a lower S/N level, and it is only significantly detected in the region of highest H_2 flux south-west of the nucleus. The line ratio 1–0 S(3)/1–0 S(1) appears to be high ($\gtrsim 1$) south-west of the

nucleus which would suggest that excitation by thermal processes may dominate (e.g. Rodríguez-Ardila et al. 2004). However, the 1–0 S(3) line is in a spectral region affected by telluric absorption and therefore we cannot robustly determine the line ratios. For the reason given in the previous sentence, we will use the 1–0 S(1) H_2 line for our diagnostics and will refer to it as H_2 in the following discussion. Another option is to compare the line ratios of $\text{H}_2/\text{Br}\gamma$. In the entire region where $\text{Br}\gamma$ is detected ($r < 0.8$ arcsec) $\text{H}_2/\text{Br}\gamma < 1$, but $\text{Br}\gamma$ is not significantly detected outside the PSF. H_2 is typically more intense relative to $\text{Br}\gamma$ in Seyfert 2 galaxies than in starburst galaxies which may be an indication that AGN make an important contribution to the excitation mechanisms of molecular gas (Riffel, Rodríguez-Ardila & Pastoriza 2006). In our source, the ratio is lower than one in the centre, but higher than one for the outer regions. This could indicate that in the central regions non-thermal processes contribute to the excitation of H_2 while in the outer regions we see an increased contribution from shock excitation (Valencia et al. 2012; Mazzalay et al. 2013).

The H_2 line flux was integrated to determine the luminosity and estimate the total molecular gas mass. The redshifted emission line component is also integrated to determine its luminosity. Determining the total gas mass requires first the conversion of H_2 luminosity to warm H_2 gas mass. To then determine the total gas mass, it is necessary to know the ratio of cold gas mass to warm gas mass. Converting the 1–0 S(1) H_2 luminosity to total gas mass is not trivial. There are several estimates for a conversion between these two values from studies which compare the H_2 luminosity with total gas mass derived from sub-mm observations of CO for various samples of galaxies (e.g. Dale et al. 2005; Müller Sánchez et al. 2006; Mazzalay et al. 2013).

Here we use the conversion from Mazzalay et al. (2013), who determine the conversion factor by studying the inner regions ($r < 300$ pc) of six nearby galaxies (consisting of low-luminosity AGN, Seyferts and one quiescent galaxy). They find that a factor

Table 2. Estimates for H₂ flux, H₂ luminosity and total molecular gas mass for various spatial regions in the galaxy. The spatial region is defined by the radius of the circular aperture where the flux is integrated. For the redshifted emission, the region of integration is 0.7 arcsec × 0.7 arcsec.

Spatial region	Molecular gas mass estimates		
	Flux (W m ⁻²)	Luminosity (erg s ⁻¹)	Total molecular gas mass (M _⊙)
$r < 3.5$ arcsec	1.4×10^{-18}	2×10^{38}	5.8×10^7
$r < 1.25$ arcsec (KDC)	8.4×10^{-19}	1×10^{38}	3.4×10^7
Redshifted emission	4.2×10^{-20}	5.5×10^{36}	1.7×10^6

of $\beta = 1174 M_{\odot}/L_{\odot}$ provides a good correlation between the independent estimates of molecular gas mass (from CO observations and from H₂ observations):

$$\frac{M_{\text{gas}}}{M_{\odot}} \sim 1174 \times \frac{L_{1-05(1)}}{L_{\odot}}, \quad (2)$$

where M_{gas} is the total molecular gas mass. We do the calculations in the masked flux map so that we are confident that we are measuring the flux in H₂. Therefore, the values we obtain are a lower estimate for the total flux. Extinction will also lower the H₂ flux we measure with respect to its intrinsic value. Pa α is not within the wavelength range of our observations and therefore we are not able to derive accurate line ratios from the hydrogen recombination lines. However, the effect of extinction will also make our measured value of H₂ flux to be a lower estimate for the total flux. The estimates are summarized in Table 2.

3.4 Stellar population

The distribution and kinematics of [Fe II] indicate dynamics distinct from the ionized species of [Si VI] and [Ca VIII] which trace outflowing gas (Fig. 9). As described in Section 3.2.2, we argue that supernova shocks are the main excitation mechanism for [Fe II]. As the [Fe II] emission is restricted to the region of the distinct core, with an underlying counter-rotating velocity component, it is likely that these supernova events are a consequence of the formation of the stellar counter-rotating core. The supernova rate (SNR) we are observing results from the stellar evolution of the counter-rotating population of stars which were formed from the initial inflow of gas. Using the measured [Fe II] flux and stellar evolution models, we can derive constraints on the age of the stellar population. The [Fe II] flux we measure is higher than our previous estimate (Raimundo et al. 2013), mainly due to the larger field of view, which allow us to determine more accurately the extent of the counter-rotating core, and due to the higher S/N in the [Fe II] line emission in our new data. Using equation (2) in Raimundo et al. (2013) taken from Rosenberg, van der Werf & Israel (2012), and a theoretical ratio of [Fe II] λ 1.64 μ m/[Fe II] λ 1.26 μ m = 0.7646 (Nussbaumer & Storey 1988), we can convert the spatially integrated [Fe II] luminosity into a supernova rate estimate:

$$\log \frac{\text{SNR}}{[\text{yr}^{-1}]} = (0.89 \pm 0.2) \times \log \frac{L_{[\text{Fe II}]\lambda 1.64 \mu\text{m}}}{0.7646 [\text{erg s}^{-1}]} - 36.19 \pm 0.9, \quad (3)$$

which gives $\text{SNR} = 1.9 \times 10^{-2} \text{ yr}^{-1}$ in the region of the distinct core. To determine the age of the stars which would produce the SNR we currently observe, we used the evolutionary synthesis code STARS (Sternberg 1998; Thornley et al. 2000; Sternberg, Hoffmann & Pauldrach 2003), which models the evolution of individual stellar clusters. We evolved a stellar population using STARS to determine the predicted SNR and K -band luminosity for a specific stellar age,

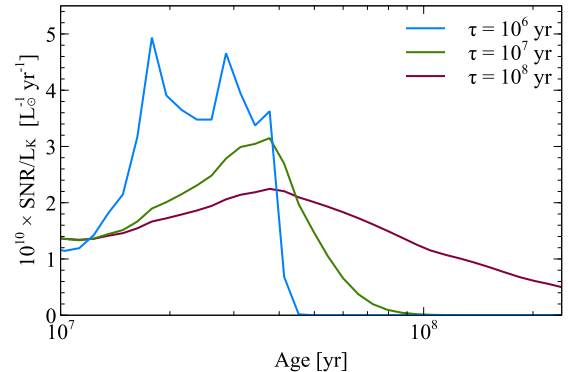


Figure 19. STARS theoretical profiles of the SNR/ L_K ratio as a function of stellar age for three different star formation decay time-scales (τ).

similar to the analysis in Raimundo et al. (2013). We assume two possible values of 1 and 10 Myr as the characteristic exponential decay time-scales of the star formation (τ) and a Salpeter initial mass function for the stellar evolution modelling. We calculate the luminosity in the K band from the absolute magnitude using the relation in Davies et al. (2007): $M_K = -0.33 - 2.5 \log L_K$, where L_K is the total luminosity in the K band in units of bolometric solar luminosity (L_{\odot}). We obtain $L_K = 5.1 \times 10^7 L_{\odot}$ in the region of the distinct core. To use STARS as a diagnostic on the stellar age, we compare results normalized to our K -band luminosity as in Davies et al. (2007), i.e. we compare the SNR/ L_K ratio predicted by STARS and the one we observe. In Fig. 19, we show the predicted evolution of the SNR/ L_K as a function of stellar age. Considering the higher SNR obtained from our new data and the K -band luminosity within the distinct core ($r < 1.25$ arcsec), we estimate $10^{10} \times \text{SNR}/L_K \sim 3.7$ which indicates a stellar age of around 40 Myr and a mass-to-light ratio of $M/L_K = 0.7 M_{\odot}/L_{\odot}$ for a characteristic star formation time-scale $\tau = 10^6$ yr, which agree within the uncertainties with our previous estimate of 65 Myr (Raimundo et al. 2013). Assuming that all the [Fe II] flux is due to supernova events provides an upper limit estimate for the SNR. If the AGN contributes to the excitation of [Fe II], then the values for the stellar age which we estimate are lower limits. What we can conclude from this analysis is that there is strong indication of at least one recent starburst in the nucleus of MCG-6-30-15, with an age younger than 100 Myr, most likely close to 50 Myr.

From the STARS modelling, we can determine the current mass in stars for our SNR and L_K . Within the KDC, we calculate that the mass in stars is $M_* \sim 10^6 M_{\odot}$ (considering $\tau = 10^6$ or 10^7 yr), while the molecular gas mass estimated from the previous section is $M_{\text{mol KDC}} = 3.4 \times 10^7 M_{\odot}$ which is significantly larger. This indicates that the starburst which formed the KDC did not exhaust the total gas mass which was accreted to the centre of the galaxy. It

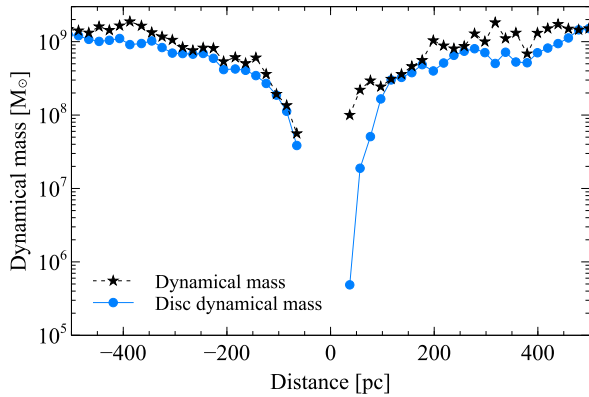


Figure 20. Dynamical mass (total enclosed mass) as a function of distance from the black hole based on the H_2 kinematics for two types of distributions: first considering that the velocity dispersion makes a significant impact in the dynamics (black points) and second considering that the distribution is approximately a disc (blue points).

is possible that another starburst will occur in the near future from the molecular gas reservoir we observe.

3.5 Dynamical modelling

One of our goals is to understand the dynamics in the central regions of MCG–6–30–15. In our previous work, we observed that the second velocity moment of the line-of-sight velocity distribution was not very sensitive to the presence of a black hole with mass lower than $\sim 10^7 M_\odot$ (Raimundo et al. 2013). Here we explore various approaches to better constrain the black hole mass, based on the stellar and gas dynamics. The ionized gas dynamics show that this gas component is affected by the AGN outflow and possibly supernova shocks as well and therefore is not a good tracer of the underlying gravitational potential. The molecular gas however rotates in a disc-like structure, and although there is an area of the map which shows disturbed dynamics (and possible inflow), most of the H_2 dynamics appears to be dominated by the central gravitational potential. Since the H_2 emission is consistent with rotation in a thin disc, its velocity distribution can be used as a first estimate of the enclosed mass:

$$M_{\text{dyn}}(r) = \frac{(V_{\text{obs}}/\sin(i))^2 + 3\sigma^2}{G} r, \quad (4)$$

where V_{obs} is the observed rotational velocity, i is the disc inclination (with $i = 0$ deg being face-on and $i = 90$ deg being edge-on), σ is the velocity dispersion of the gas and r is the distance from the centre of the galaxy (which is defined as the AGN position). If we assume that the gas is rotationally dominated and the velocity dispersion contribution to the dynamics is negligible (in Fig. 14 we see that $V/\sigma \sim 3$ for an inclination of 61 deg), then

$$M_{\text{dyn}}(r) = \frac{V_{\text{obs}}^2}{G \sin^2(i)} r. \quad (5)$$

An estimate of the total (stars + gas + dark matter) enclosed dynamical mass at various radii is obtained from the H_2 kinematical modelling (Fig. 20). If we consider the innermost radius where we can get an accurate measurement of the H_2 dynamics, and use the average velocity and velocity dispersion measured at both sides of the nucleus along the H_2 PA, and the inclination measured from DISKFIT, we obtain an upper limit for the enclosed mass within the PSF of our data, $r < 0.5$ arcsec ($r \lesssim 80$ pc) and therefore for the

black hole mass of $M_{\text{enc}} < 1.8 \times 10^8 M_\odot$ or if we consider the velocity dispersion negligible: $M_{\text{enc}} < 7.8 \times 10^7 M_\odot$.

3.5.1 Jeans anisotropic model

To model the overall potential of the galaxy, we use the Jeans anisotropic models (JAM) method (Cappellari 2008). The general goal in dynamical modelling is to determine the underlying gravitational potential, or the mass, from the position and velocity of a sample of stars. The Jeans equations reduce the problem of determining the distribution function (position and velocity) of stars by focusing on determining only the velocity moments of the distribution function. Axisymmetry is assumed to reduce the complexity of the problem: in cylindrical coordinates, the symmetry is assumed in relation to the coordinate ϕ . Furthermore a ‘semi-isotropy’ condition is often assumed, where $\overline{v_R^2} = \overline{v_z^2}$. In the anisotropic Jeans solutions (Cappellari 2008), the assumptions are not as restrictive, and a constant anisotropy factor is included to account for possible anisotropies: $b = \overline{v_R^2}/\overline{v_z^2}$.

As input for the dynamical model, we first start by modelling the galaxy surface brightness from the stellar emission. The surface brightness is more accurately modelled in the H band, the S/N is higher in the CO absorption bands detected in this waveband and therefore the stellar continuum is better isolated. We use the Multi-Gaussian Expansion (MGE) method of Emsellem, Monnet & Bacon (1994) and the MGE fitting software developed by Cappellari (2002) to parametrize our surface brightness in terms of Gaussians. To determine the MGE decomposition, we used the H -band image with the hydrogen broad $\text{Br}\gamma$ and the AGN continuum removed, from our method of AGN and stellar continuum decomposition based on the equivalent width of the CO absorption lines (see Section 2.3 and Fig. 2). The stellar continuum data cube is then integrated in wavelength to obtain the stellar emission at each pixel of the image. In the MGE Gaussian decomposition, the minimum Gaussian axial ratio determines the minimum inclination allowed in the subsequent dynamical model. We therefore explore the χ^2 variation of the Gaussian fit as the minimum axial ratio is changed and set a limit for the minimum ratio allowed in MGE, as suggested in Cappellari (2002). For the H band, the minimum projected axial ratio is set at 0.56. The best-fitting Gaussians are plotted in Fig. 21 (left). To model the inner regions of the field of view, we use our previous H -band data at resolution of 0.1 arcsec. The MGE modelling for the nuclear region is shown in Fig. 21 (right).

The MGE parameters which characterize the Gaussians are converted to the units required by the JAM code using the guidelines for the MGE FIT SECTORS package released by Michele Cappellari. The input for JAM is then the stellar surface brightness based on the MGE parametrization (peak surface brightness, dispersion and observed axial ratio of each Gaussian), the inclination, the distance, the observed kinematics and its associated uncertainties and (optionally) the black hole mass.

To determine the first moment of the line-of-sight velocity distribution, the line-of-sight velocity, further constraints are needed because one needs to separate the contribution of ordered and random motions. To compare the second moments, the problem has essentially three unknown parameters, the mass-to-luminosity ratio (M/L), the anisotropy $\beta = 1 - 1/b$ and the inclination i . M/L is weakly dependent on the anisotropy. However, there is a degeneracy between the inclination and β . As discussed in Cappellari (2008), the inclination can be recovered if we assume certain observational constraints on β , as in their sample of fast rotators for example, or vice versa. A dynamical signature of the presence of the black hole

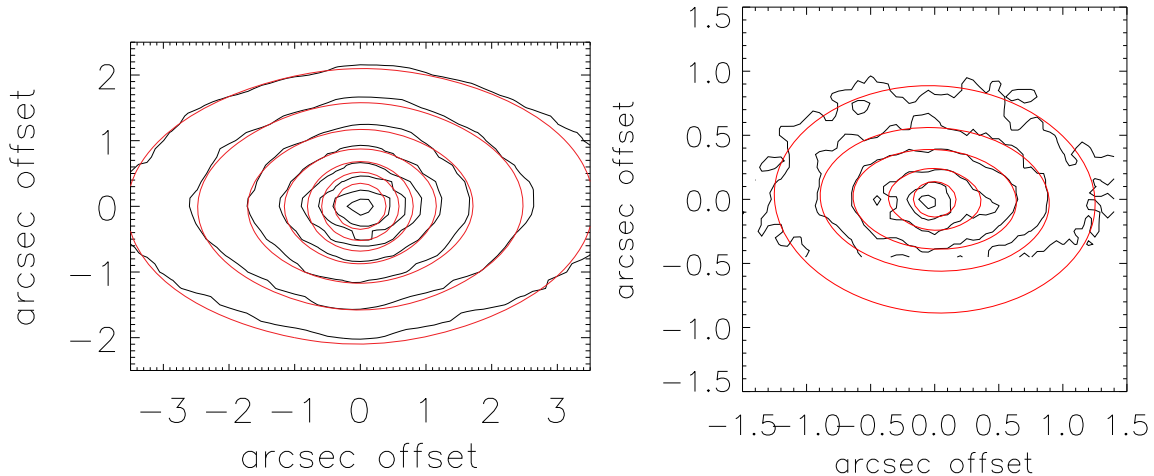


Figure 21. MGE best-fitting parametrization (red contours) for the H -band stellar continuum (black contours). Left: larger field of view. Right: fit to the nuclear regions using the higher resolution data of Raimundo et al. (2013).

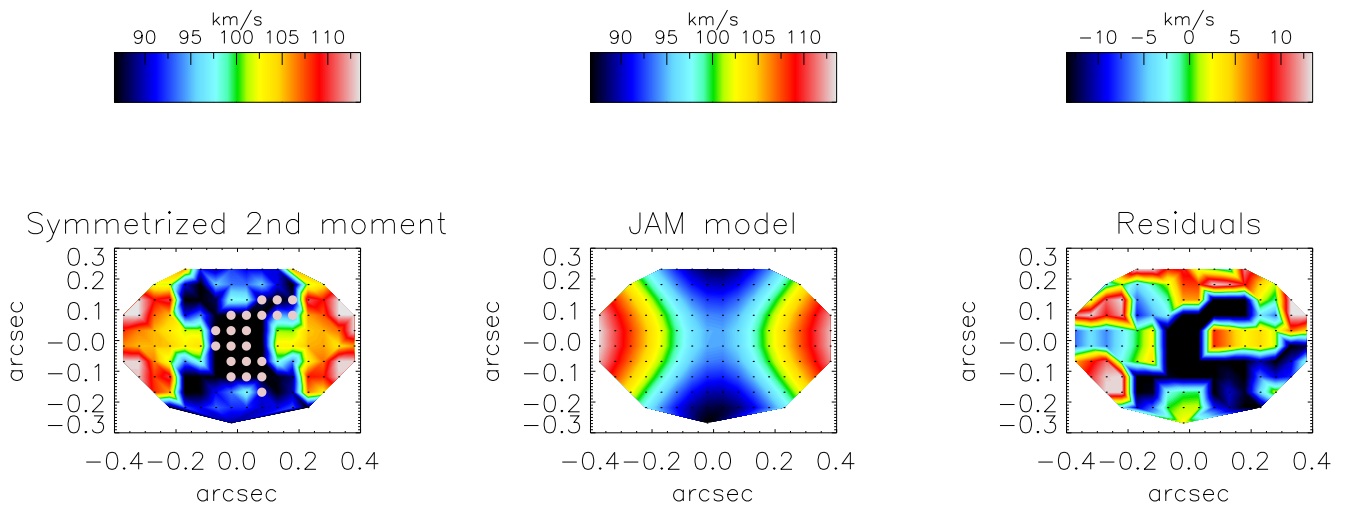


Figure 22. JAM modelling. The second moment ($V_{\text{rms}} = \sqrt{V^2 + \sigma^2}$) of the stellar velocity distribution (left-hand panel) is compared with the output from the model (middle panel). The residuals are shown in the right-hand panel.

would be an increase of the stellar velocity dispersion in the centre of the galaxy. This would be indicated by a central increase in the observed second velocity moment ($V_{\text{rms}} = \sqrt{V^2 + \sigma^2}$). However, for the low black hole masses ($<10^7 M_{\odot}$), this increase is expected to be present at very small radii and it is not observed in our data. In Raimundo et al. (2013), we determined an upper limit for the black hole mass, which was a more robust constraint considering the information we had on the source. In these new data, we are probing even larger radii (the H -band spatial resolution in this work is 0.6 arcsec, higher than the 0.1 arcsec in Raimundo et al. 2013). However, with the molecular gas information, we have a new constraint on the galaxy inclination if we consider that the H_2 gas is in circular orbits, and can fix the inclination to 61 deg in our dynamical model. We used the H -band data at resolution of 0.1 arcsec from Raimundo et al. (2013) as input for the new JAM modelling. The model takes in the maps for the stellar velocity and stellar velocity dispersion and the errors in these parameters determined by Monte Carlo simulations. We restricted our fit to the inner $r < 0.4$ arcsec where the black hole potential will have the highest impact on the

second moment of the line-of-sight velocity. The inclination is fixed at 61 deg and the M/L , β and M_{BH} are allowed to vary. The bins which show the highest errors in velocity and velocity dispersion due to the strong AGN continuum were masked out of the fit to ensure that they would not bias our result and are represented in the plot by the grey filled circles. The observed second velocity moment ($V_{\text{rms}} = \sqrt{V^2 + \sigma^2}$) is compared with the projected (and convolved with the instrumental PSF) V_{rms} from the JAM modelling, and we use the least-squares minimization algorithm MPFIT (Markwardt 2009) to find the best-fitting set of parameters. The maps for the best-fitting result are shown in Fig. 22. The best-fitting black hole mass is $2.5 \times 10^7 M_{\odot}$; however, a lower black hole mass or even a zero black hole mass is consistent within a 3σ error. Although the absolute values for the model parameters may be affected by degeneracies, we can analyse their overall trend: the negative ($\beta < 0$) value obtained indicates a tangential anisotropy in the regions close to the black hole (observed in other galaxies with counter-rotating components as well; Cappellari et al. 2007), and the M/L ratio is higher than what was determined from the STARS code modelling

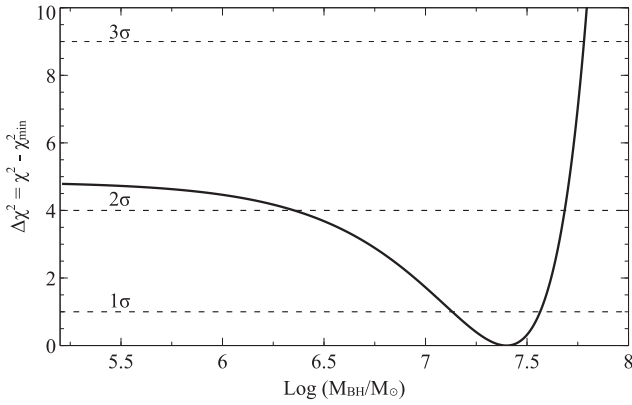


Figure 23. $\Delta\chi^2$ as a function of black hole mass for the JAM fit. Confidence levels for a χ^2 distribution with one degree of freedom are indicated by the horizontal dashed lines.

in Section 3.4, which is consistent considering that there may be a contribution from dark matter and/or gas to the total mass. To evaluate the confidence limits for the black hole mass, we determine the chi-square difference as a function of black hole mass. This method relies on estimating $\Delta\chi^2 = \chi^2 - \chi_{\min}^2$, which is a quantity that only depends on the number of ‘interesting’ parameters and not on the total number of parameters or degrees of freedom used in the initial fit (Avni 1976). In our case, the only ‘interesting parameter’ is the black hole mass and for each fixed value of M_{BH} we minimize χ^2 over the remaining parameters. The result is shown in Fig. 23 with the confidence limits $\Delta\chi^2 = 1$ (1σ), $\Delta\chi^2 = 4$ (2σ) and $\Delta\chi^2 = 9$ (3σ) considering a χ^2 distribution with one degree of freedom. Our best-fitting black hole mass assuming a fixed inclination of 61 deg is $M_{\text{BH}} = 2.5^{+2.3}_{-2.3} \times 10^7 M_{\odot}$ with the confidence limits referring to a 2σ (95.4 per cent) confidence level. As can be seen from Fig. 23, our data are not very sensitive to lower black hole masses and they are essentially consistent within 3σ with values down to zero black hole mass. Therefore, the strongest constraint from our modelling is a 3σ upper limit for the black hole mass of $M_{\text{BH}} < 6 \times 10^7 M_{\odot}$.¹

3.6 The kinematically distinct core

To determine the size of the distinct core, we use the stellar velocity map and define as the radius of the KDC the spatial region where the superposition of the two velocity components has a local minimum (as in McDermid et al. 2006). We determine a size of $r \sim 1.25$ arcsec (200 pc) for the KDC in MCG–6–30–15. The H_2 distribution extends to larger radii ($r < 600$ pc) than the counter-rotating stellar core ($r < 200$ pc). If the stars of the counter-rotating core formed *in situ* and from this gas, they are expected to trace the highest gas density which may explain why they are confined to a smaller diameter than the gas. The counter-rotating system could have a larger diameter but not be observable in the infrared – we are limited to observing the regions where the luminosity of the counter-rotating stars dominates over the stars corotating in the main body of the galaxy. In each position of the field of view, the velocity distribution we observe is a superposition of the stars in the KDC and the stars in the main body of the galaxy, weighted by their relative contributions to the total light at that particular position. We explored the possibility of

decomposing the spectra into two line-of-sight velocity components at every pixel. We modified pPXF to include two different sets of templates, one set to model the stars in the KDC and another set to model the stars in the main body of the galaxy, similar to what has been done in Coccato et al. (2011) and Johnston et al. (2013). Due to the small difference in velocities between the two components, in particular in the central 2 arcsec, it is not possible to obtain an unambiguous decomposition for the full field of view without further constraints. We also notice a significant dependence of the final result on the initial parameters chosen and therefore do not attempt to fit different stellar populations or determine the line-of-sight distribution for the two components independently. Instead, we follow a different approach to determine the relative contribution of each of the components to the total light, which will give us an idea of how much the KDC contributes to the light outside its apparent size. We assume that if the counter-rotating stars formed from the molecular gas, their dynamics should be similar; therefore, the line-of-sight velocity can be approximated by a superposition of a component with the dynamics of the H_2 disc and another component with dynamics similar to the main body of the galaxy (which we consider to be the stellar dynamics at $r > 2$ arcsec). We build two different templates: one which is a convolution of K-type stellar templates with a Gaussian kernel with the velocity and velocity dispersion of the H_2 gas profile, and another one which is a convolution of K-type stellar templates with a Gaussian kernel with velocity and velocity dispersion of the stars between $2 \text{ arcsec} < r < 3 \text{ arcsec}$. The two templates are used as input to pPXF. The velocity and velocity dispersion of the KDC template are allowed to vary within the measurement errors while the parameter space for the velocity and velocity dispersion of the main galaxy template is broader to take into account the fact that even at $r > 2$ arcsec the line-of-sight distribution may still be affected by the KDC component. We find that the galaxy spectra can be well reproduced by a combination of these two templates. For radius $r \gtrsim 1$ arcsec, the contribution of the KDC component to the light is ~ 20 – 30 per cent. Within $r < 1$ arcsec, the relative contribution of the templates is harder to determine but we observe that the KDC component dominates and is responsible for ~ 60 – 80 per cent of the light. We also obtain higher absolute velocities for the main galaxy component, $V \sim 50 \text{ km s}^{-1}$ at $r \sim 2$ arcsec along the major axis compared with $V \sim 30 \text{ km s}^{-1}$ when fitting the line-of-sight velocity with just one component. This indicates that the rotation curve for the main body of the galaxy has a higher absolute velocity than what we measure in Fig. 14 for the combined KDC + main galaxy line-of-sight velocity distribution, which is expected since the counter-rotation of the KDC will cause a shift in the centroid of the absorption line profiles.

3.6.1 Formation of the KDC

We use the observations and results of this work to constrain the formation scenarios for the KDC. To fully constrain the origin and age of the distinct core, an important diagnostic would be to determine the age and metallicities of the stellar populations in the counter-rotating core and in the main body of the galaxy. The scenario where gas accretion and subsequent *in situ* star formation occurs implies that the stellar age of the counter-rotating component is always younger than the main body of the galaxy. In the case of minor mergers as the origin for the stars and gas in the distinct core, the stellar population can be younger or older than the population in the main body of the galaxy. High spatial resolution optical observations which could model the stellar populations would allow

¹ Our estimates are consistent with the black hole mass measurement of $(1.6 \pm 0.4) \times 10^6 M_{\odot}$ (Bentz et al. 2016) from a recent reverberation mapping campaign which was published after the submission of this paper.

us to set better constraints on the formation scenario for the KDC. However, with the information we currently have, we can exclude some of the formation mechanisms and derive conclusions about the recent past of MCG–6–30–15 and its AGN activity.

We observe four key features. (1) The KDC is relatively small (diameter of less than 1 kpc). (2) The molecular gas is also counter-rotating in relation to the main body of the galaxy. (3) There is evidence, from our [Fe II] and SNR discussion and from UV observations (Bonatto et al. 2000), that there are traces of recent star formation (age < 100 Myr) in this galaxy. (4) A dust lane is observed which points towards a past dynamical interaction.

There are various hypotheses for the formation of KDC which we can exclude as unlikely in the case of our galaxy: (a) the size of the KDC is too small to have been formed during a major merger; (b) the counter-rotating orientation and the presence of molecular gas indicate that dissipation was important in the formation of the KDC; if a merger occurred, it most likely was a minor merger and involved gas; and (c) the scenarios for an internal origin for the KDC are extremely unlikely in our galaxy; the lack of a stellar bar and the presence of a large quantity of counter-rotating ionized and molecular gas in addition to a counter-rotating stellar core indicate that the origin of the KDC is not internal. Our observations are in line with the scenario of the KDC being formed by recent accretion of gas into the nuclei and subsequent *in situ* star formation, as proposed by McDermid et al. (2006) for the formation of small KDCs. It is unclear if the KDC was formed by the accretion of a small satellite galaxy or external gas accretion, induced by tidal interactions with one of its neighbours for example, which drove gas to the nuclei and subsequently formed stars. In any of these cases, we can conclude that gas with an external origin was accreted into the nucleus.

There are several spiral galaxies (e.g. NGC 5719, Coccato et al. 2011; NGC 4138, Pizzella et al. 2014), and S0 galaxies (e.g. NGC 3593, NGC 4550 – Coccato et al. 2013 and NGC 4191 – Coccato et al. 2015), which show counter-rotating ionized gas in addition to counter-rotating stars, although these counter-rotating stars are typically on the form of large-scale discs and not small cores. For these galaxies, the gas has an external origin, and for S0 galaxies in particular the formation of the counter-rotating stars involves accretion of external gas into an already existing gas-free disc and subsequent *in situ* star formation (e.g. NGC 3593 – Bertola et al. 1996, a galaxy which also shows counter-rotating molecular gas – García-Burillo et al. 2000).

3.6.2 The environment of MCG–6–30–15

The environment of MCG–6–30–15 is important to determine the origin of the gas whose remnants we observe in the form of the H₂ gas distribution and that possibly formed the stellar counter-rotating core. There is a strong indication that MCG–6–30–15 is in a small group based on the distance to its fourth nearest neighbour, which is only 4.1 Mpc (from the 2MASS redshift survey), much smaller than what is found for isolated galaxies (15–30 Mpc). It is likely that these neighbours are the source of the recently accreted gas. H I images could determine the gas distribution in the outskirts and neighbouring regions of the galaxy but they are not available in the literature. Tentative evidence for dynamical interactions comes from the Bonatto et al. (2000) identification criteria which include MCG–6–30–15 in the set of nearby disturbed galaxies and from the presence of a dust lane in MCG–6–30–15 which is in line with a possible past interaction between this galaxy and one of its neighbours.

3.6.3 Implications for AGN fuelling

From a study of the distribution of gas in the inner kpc of S0 galaxies, Davies et al. (2014) find that the AGN in these galaxies are typically fuelled by external gas accretion. The observations and results for MCG–6–30–15 reinforce this scenario of AGN fuelling in S0 galaxies. In MCG–6–30–15, we observe a small stellar counter-rotating core and most importantly counter-rotating molecular gas which indicates that accretion of external gas occurred in this galaxy. The counter-rotating molecular gas has significantly replenished the AGN fuelling reservoir at scales of hundreds of parsecs, with a total mass of $3.4 \times 10^7 M_{\odot}$ in the central 400 pc. We also see that the molecular gas is present at radius $r \lesssim 50$ –100 pc which indicates that this external gas accretion event was able to drive gas to the central hundred parsecs. Considering these observations, we conclude that external accretion has likely provided the gas needed to replenish the AGN fuelling reservoir in MCG–6–30–15.

MCG–6–30–15 was famously the first galaxy to show a broad Fe K α emission line in the X-ray spectrum (Tanaka et al. 1995) which allowed the black hole spin to be measured. The most recent measurements indicate a high black hole spin of $a > 0.98$ (Brenneman & Reynolds 2006). Having a molecular gas reservoir counter-rotating in relation to the main body of the galaxy provides an interesting laboratory for tests on accretion physics. From theoretical models, the black hole spin increases due to continuous accretion of material with similar angular momentum. If the black hole has been accreting from the counter-rotating gas for the past 50 Myr or more, it could mean that the black hole is currently decreasing its spin. Middleton et al. (2016) find a misalignment between the inclination of the inner accretion disc and the host galaxy large-scale stellar disc. They suggest that this misalignment could be related with the AGN in MCG–6–30–15 being fuelled by an external accretion event, which is supported by our findings.

In S0 galaxies such as MCG–6–30–15, KDCs are relatively rare (< 10 per cent; Kuijken et al. 1996). Out of the tens of KDCs discovered and published in the literature, MCG–6–30–15 has one of the highest AGN X-ray luminosities ($L_X(2\text{--}10\text{ keV}) = 4 \times 10^{42} \text{ erg s}^{-1}$). Most of the remaining galaxies are quiescent and the ones with active nuclei have lower X-ray luminosities typical of LINERs. As small KDCs can only be detected with high spatial resolution observations, we may be severely underestimating the number of galaxies with KDCs. Integral field spectroscopy observations are one of the best techniques to resolve the small KDC; however, galaxies which host luminous AGN are often not considered as targets for integral field spectroscopy studies due to AGN contamination to the emission from the galaxy. We are therefore likely biased to low-luminosity AGN or quiescent galaxies. MCG–6–30–15 is therefore a unique and important case study since it has both a bright AGN and a small KDC.

Our current best theory to explain the formation of the distinct core is that earlier than 50–100 Myr ago MCG–6–30–15 accreted external gas from a neighbour or had a minor merger with a small gas-rich satellite galaxy. Out of this interaction, gas with a distinct angular momentum was driven to the centre of the galaxy, settling on a disc counter-rotating with respect to the galaxy's main body rotation. From this gas, a younger stellar population formed which generated the stellar KDC we observe. Possibly this gas formed or replenished the AGN fuelling reservoir at scales of hundreds of parsecs, and we currently observe a remnant of the initial gas. A redshifted component in the H₂ velocity in our data, if proven to be associated with the dust lane, would indicate that inflow from this disc of gas down to the centre of

the galaxy may provide fuelling to the black hole in the near future.

4 CONCLUSIONS

In this work, we analysed the central 1–2 kpc of the active galaxy MCG–6–30–15 using new SINFONI observations in the H and K bands and VIMOS observations $\lambda[4200\text{--}6150]$ Å. We mapped for the first time the molecular gas distribution traced by the H_2 emission and the extent of the counter-rotating core first detected in the H band (Raimundo et al. 2013). Our main goal was to investigate if the formation of the stellar counter-rotating core was associated with inflow of gas into the centre of the galaxy. Our main conclusions can be summarized as follows.

(i) The molecular gas is in a counter-rotating disc. The molecular gas shows counter-rotation with respect to the main body of the galaxy similar to what is observed in the counter-rotating stars but more extended (detected out to $r \sim 600$ pc). If the stars of the counter-rotating core formed from this gas, the fact that they are confined to a smaller diameter could trace the regions of higher gas density. Alternatively, the counter-rotating stellar core could indeed extend further out but we only observe the regions where the luminosity of the counter-rotating stars dominates over the main body of the galaxy. We determine that the contribution of the counter-rotating stars to the total light is $\sim 20\text{--}30$ per cent for $r \gtrsim 1$ arcsec. The molecular gas dynamics are well modelled by a rotating disc with inclination ~ 61 deg assuming circular rotation and the PA of the molecular gas is similar to that of the stars in the distinct core. The counter-rotating orientation suggests that dissipative processes were important in the formation of the distinct core. An H_2 residual redshifted component is observed to the west of the nucleus, coinciding with the peak in the H_2 flux. This component has a velocity of 120 km s^{-1} and velocity dispersion similar to the bulk of the H_2 disc. The redshifted component seems to trace the dust lane which is observed south of MCG–6–30–15’s and just below our line of sight towards the nucleus. According to this geometry, the redshifted component would be associated with gas moving towards the nucleus of the galaxy. If this feature indicates counter-rotating gas inflow to the centre of the galaxy remains to be investigated with higher sensitivity observations.

(ii) The ionized gas shows outflows. The various ionized gas tracers indicate a combination of outflows and counter-rotation when circular motions dominate. The narrow-line $\text{Br}\gamma$ emission originates in the nuclear region and is very compact, while narrow $\text{H}\beta$ is more extended ($r < 400$ pc). They both show counter-rotation. The $[\text{Ca VIII}]$ dynamics is dominated by non-rotational motions, and the spectra show two emission line components: a redshifted and a blueshifted one at each spatial position which trace the approaching and receding sides of an outflow cone. From the dynamical analysis, we conclude that $[\text{Ca VIII}]$ is tracing an outflow with velocity $\sim 100 \text{ km s}^{-1}$, where the redshifted component of the outflow dominates the flux we observe. The $[\text{O III}]$ emission shows disturbed dynamics at $\sim \text{kpc}$ scales which indicates that the $[\text{Ca VIII}]$ detected outflow may extend to larger radii. $[\text{Fe II}]$ emission presents velocities above what is expected from the stellar rotation but also distinct from $[\text{Ca VIII}]$. We argue that $[\text{Fe II}]$ is excited by supernova shocks and is tracing the local dynamics. From its flux, we estimate that the star formation in the distinct core happened ~ 50 Myr ago.

(iii) The black hole mass is constrained dynamically. From the dynamics of the H_2 emission, we can determine the total enclosed mass in the inner 80 pc to be $M_{\text{enc}} < 7.8 \times 10^7 M_{\odot}$ which sets an

upper limit for the M_{BH} . Using JAM and fixing the inclination to 61 deg as indicated from the molecular gas dynamics, we determine a best-fitting black hole mass of $M_{\text{BH}} = 2.5_{-2.3}^{+2.3} \times 10^7 M_{\odot}$ with 2σ (95.4 per cent) confidence limits. As our data are not very sensitive to lower black hole masses, the strongest constraint from our modelling is a 3σ upper limit for the black hole mass of $M_{\text{BH}} < 6 \times 10^7 M_{\odot}$.

(iv) The counter-rotating core was formed by external gas accretion. With the data presented here, we improved on the size measurement of the counter-rotating core first estimated in Raimundo et al. (2013) and determine that the core has a diameter of ~ 400 pc extending out to a radius of $r \sim 1.25$ arcsec. The results from this work point to a scenario where the KDC was formed by external gas accretion. The KDC is small, molecular gas is present and counter-rotating in relation to the main body of the galaxy, there are traces of recent star formation (age < 100 Myr) in this galaxy and a dust lane is observed which points towards a past dynamical interaction. Currently, a molecular gas mass of $M_{\text{gas}} = 3.4 \times 10^7 M_{\odot}$ is present in the central 400 pc of MCG–6–30–15. The fact that we observe counter-rotating molecular gas at radius $r \lesssim 50\text{--}100$ pc indicates that this external gas accretion event was able to drive gas to the central hundred parsecs. Our observations agree with what was found by Davies et al. (2014), that AGN in S0 galaxies are typically fuelled by external accretion.

The results in this work suggest a scenario where the formation of the stellar KDC is associated with gas inflow. External gas (from a galaxy neighbour or part of a minor merger with a gas-rich satellite) was driven into the centre of the galaxy where it settled in the form of a counter-rotating disc in the equatorial plane of the galaxy. This event provided gas to replenish the AGN fuelling reservoir on scales of hundreds of parsecs. KDC formation when associated with gas can provide a tracer for the presence of fresh gas for AGN fuelling.

ACKNOWLEDGEMENTS

The authors would like to thank the referee, Cristina Ramos Almeida, for a thorough reading of the paper and for the constructive comments and suggestions which improved this work. They would also like to thank Michele Cappellari, Craig Markwardt, Jeremy Sanders and Kristine Spekkens for making their codes and/or software available to the community. The plots in this paper were produced with the plotting package `VEUSZ` by Jeremy Sanders. ACF acknowledges support from ERC Advanced Grant 340442. PG acknowledges support from STFC (grant reference ST/J003697/2). This research has made use of the NASA/IPAC Extragalactic Database (NED), which is operated by the Jet Propulsion Laboratory, California Institute of Technology, under contract with the National Aeronautics and Space Administration. In this work, we used data obtained as part of the Two Micron All Sky Survey (2MASS), a joint project of the University of Massachusetts and the Infrared Processing and Analysis Center/California Institute of Technology, funded by the National Aeronautics and Space Administration and the National Science Foundation. This research has made use of NASA’s Astrophysics Data System.

REFERENCES

- Algorry D. G., Navarro J. F., Abadi M. G., Sales L. V., Steinmetz M., Piontek F., 2014, MNRAS, 437, 3596
 Avni Y., 1976, ApJ, 210, 642
 Ballantyne D. R., Weingartner J. C., Murray N., 2003, A&A, 409, 503

- Bentz M. C., Cackett E. M., Crenshaw D. M., Horne K., Street R., Ou-Yang B., 2016, *ApJ*, 830, 136
- Bertola F., Buson L. M., Zeilinger W. W., 1992, *ApJ*, 401, L79
- Bertola F., Cinzano P., Corsini E. M., Pizzella A., Persic M., Salucci P., 1996, *ApJ*, 458, L67
- Blustin A. J., Page M. J., Fuerst S. V., Branduardi-Raymont G., Ashton C. E., 2005, *A&A*, 431, 111
- Bois M. et al., 2011, *MNRAS*, 416, 1654
- Bonatto C., Bica E., Pastoriza M. G., Alloin D., 2000, *A&A*, 355, 99
- Brenneman L. W., Reynolds C. S., 2006, *ApJ*, 652, 1028
- Bureau M., Chung A., 2006, *MNRAS*, 366, 182
- Burtscher L. et al., 2015, *A&A*, 578, A47
- Cappellari M., 2002, *MNRAS*, 333, 400
- Cappellari M., 2008, *MNRAS*, 390, 71
- Cappellari M., Copin Y., 2003, *MNRAS*, 342, 345
- Cappellari M., Emsellem E., 2004, *PASP*, 116, 138
- Cappellari M. et al., 2007, *MNRAS*, 379, 418
- Chiang C.-Y., Fabian A. C., 2011, *MNRAS*, 414, 2345
- Coccatto L., Morelli L., Corsini E. M., Buson L., Pizzella A., Vergani D., Bertola F., 2011, *MNRAS*, 412, L113
- Coccatto L., Morelli L., Pizzella A., Corsini E. M., Buson L. M., Dalla Bontà E., 2013, *A&A*, 549, A3
- Coccatto L. et al., 2015, *A&A*, 581, A65
- Cohen M., Wheaton W. A., Megeath S. T., 2003, *AJ*, 126, 1090
- Combes F. et al., 2013, *A&A*, 558, A124
- Combes F. et al., 2014, *A&A*, 565, A97
- Dale D. A., Sheth K., Helou G., Regan M. W., Hüttemeister S., 2005, *AJ*, 129, 2197
- Davies R. I., Müller Sánchez F., Genzel R., Tacconi L. J., Hicks E. K. S., Friedrich S., Sternberg A., 2007, *ApJ*, 671, 1388
- Davies R. I., Maciejewski W., Hicks E. K. S., Tacconi L. J., Genzel R., Engel H., 2009, *ApJ*, 702, 114
- Davies R., Agudo Berbel A., Wierorke E., Ott T., Förster-Schreiber N. M., 2010, *Proc. SPIE*, 7735, 77356V
- Davies R. et al., 2011, *ApJ*, 741, 69
- Davies R. I. et al., 2014, *ApJ*, 792, 101
- Davis T. A., Bureau M., 2016, *MNRAS*, 457, 272
- Dumas G., Mundell C. G., Emsellem E., Nagar N. M., 2007, *MNRAS*, 379, 1249
- Emsellem E., Monnet G., Bacon R., 1994, *A&A*, 285
- Emsellem E. et al., 2011, *MNRAS*, 414, 888
- Ferrarese L., Merritt D., 2000, *ApJ*, 539, L9
- Fisher K. B., Huchra J. P., Strauss M. A., Davis M., Yahil A., Schlegel D., 1995, *ApJS*, 100, 69
- Forbes D. A., Ward M. J., 1993, *ApJ*, 416, 150
- García-Burillo S., Combes F., 2012, *J. Phys.: Conf. Ser.*, 372, 012050
- García-Burillo S., Sempere M. J., Combes F., Hunt L. K., Neri R., 2000, *A&A*, 363, 869
- García-Burillo S. et al., 2003, *A&A*, 407, 485
- García-Burillo S. et al., 2014, *A&A*, 567, A125
- Gebhardt K. et al., 2000, *ApJ*, 539, L13
- Häring N., Rix H.-W., 2004, *ApJ*, 604, L89
- Hernquist L., Barnes J. E., 1991, *Nature*, 354, 210
- Hicks E. K. S., Davies R. I., Maciejewski W., Emsellem E., Malkan M. A., Dumas G., Müller-Sánchez F., Rivers A., 2013, *ApJ*, 768, 107
- Hummer D. G., Storey P. J., 1987, *MNRAS*, 224, 801
- Johnston E. J., Merrifield M. R., Aragón-Salamanca A., Cappellari M., 2013, *MNRAS*, 428, 1296
- Kannappan S. J., Fabricant D. G., 2001, *AJ*, 121, 140
- Katkov I. Y., Sil'chenko O. K., Afanasiev V. L., 2014, *MNRAS*, 438, 2798
- Krajinović D., Cappellari M., de Zeeuw P. T., Copin Y., 2006, *MNRAS*, 366, 787
- Krajinović D. et al., 2011, *MNRAS*, 414, 2923
- Kuijken K., Fisher D., Merrifield M. R., 1996, *MNRAS*, 283, 543
- Le H. A. N., Kang W., Pak S., Im M., Lee J.-E., Ho L. C., Pyo T.-S., Jaffe D. T., 2011, preprint ([arXiv:1108.1499](https://arxiv.org/abs/1108.1499))
- Lira P., Arévalo P., Uttley P., McHardy I. M. M., Videla L., 2015, *MNRAS*, 454, 368
- McDermid R. M. et al., 2006, *MNRAS*, 373, 906
- Maciejewski W., 2004, *MNRAS*, 354, 892
- Magorrian J. et al., 1998, *AJ*, 115, 2285
- Marconi A., Hunt L. K., 2003, *ApJ*, 589, L21
- Markwardt C. B., 2009, in Bohlender D. A., Durand D., Dowler P., eds, *ASP Conf. Ser. Vol. 411, Astronomical Data Analysis Software and Systems XVIII. Astron. Soc. Pac., San Francisco*, p. 251
- Mazzalay X. et al., 2013, *MNRAS*, 428, 2389
- Middleton M. J., Parker M. L., Reynolds C. S., Fabian A. C., Lohfink A. M., 2016, *MNRAS*, 457, 1568
- Mouri H., Kawara K., Taniguchi Y., 2000, *ApJ*, 528, 186
- Müller Sánchez F., Davies R. I., Eisenhauer F., Tacconi L. J., Genzel R., Sternberg A., 2006, *A&A*, 454, 481
- Müller-Sánchez F., Prieto M. A., Hicks E. K. S., Vives-Arias H., Davies R. I., Malkan M., Tacconi L. J., Genzel R., 2011, *ApJ*, 739, 69
- Mundell C. G., Ferruit P., Nagar N., Wilson A. S., 2009, *ApJ*, 703, 802
- Nussbaumer H., Storey P. J., 1988, *A&A*, 193, 327
- Panuzzo P., Bressan A., Granato G. L., Silva L., Danese L., 2003, *A&A*, 409, 99
- Pizzella A., Corsini E. M., Vega Beltrán J. C., Bertola F., 2004, *A&A*, 424, 447
- Pizzella A., Morelli L., Corsini E. M., Dalla Bontà E., Coccatto L., Sanjana G., 2014, *A&A*, 570, A79
- Raimundo S. I., Davies R. I., Gandhi P., Fabian A. C., Canning R. E. A., Ivanov V. D., 2013, *MNRAS*, 431, 2294
- Ramos Almeida C., Pérez García A. M., Acosta-Pulido J. A., Rodríguez Espinosa J. M., Barrena R., Manchado A., 2006, *ApJ*, 645, 148
- Regan M. W., Sheth K., Vogel S. N., 1999, *ApJ*, 526, 97
- Reynolds C. S., Ward M. J., Fabian A. C., Celotti A., 1997, *MNRAS*, 291, 403
- Riffel R., Rodríguez-Ardila A., Pastoriza M. G., 2006, *A&A*, 457, 61
- Riffel R. A., Storchi-Bergmann T., Nagar N. M., 2010, *MNRAS*, 404, 166
- Rodríguez-Ardila A., Pastoriza M. G., Viegas S., Sigut T. A. A., Pradhan A. K., 2004, *A&A*, 425, 457
- Rodríguez-Ardila A., Prieto M. A., Viegas S., Gruenwald R., 2006, *ApJ*, 653, 1098
- Rodríguez-Zaurín J., Arribas S., Monreal-Ibero A., Colina L., Alonso-Herrero A., Alfonso-Garzón J., 2011, *A&A*, 527, A60
- Rosenberg M. J. F., van der Werf P. P., Israel F. P., 2012, *A&A*, 540, A116
- Sako M. et al., 2003, *ApJ*, 596, 114
- Sellwood J. A., Sánchez R. Z., 2010, *MNRAS*, 404, 1733
- Sellwood J. A., Spekkens K., 2015, preprint ([arXiv:e-prints](https://arxiv.org/abs/1503.07544))
- Smajić S. et al., 2014, *A&A*, 567, A119
- Spekkens K., Sellwood J. A., 2007, *ApJ*, 664, 204
- Sternberg A., 1998, *ApJ*, 506, 721
- Sternberg A., Hoffmann T. L., Pauldrach A. W. A., 2003, *ApJ*, 599, 1333
- Storchi-Bergmann T., Dors O. L., Jr, Riffel R. A., Fathi K., Axon D. J., Robinson A., Marconi A., Östlin G., 2007, *ApJ*, 670, 959
- Tanaka Y. et al., 1995, *Nature*, 375, 659
- Thornley M. D., Schreiber N. M. F., Lutz D., Genzel R., Spoon H. W. W., Kunze D., Sternberg A., 2000, *ApJ*, 539, 641
- Tsatsi A., Macciò A. V., van de Ven G., Moster B. P., 2015, *ApJ*, 802, L3
- Valencia S. M., Zuther J., Eckart A., Garcia-Marin M., Iserlohe C., Wright G., 2012, *A&A*, 544, A129
- van der Marel R. P., Franx M., 1993, *ApJ*, 407, 525
- van Dokkum P. G., 2001, *PASP*, 113, 1420
- Vasudevan R. V., Mushotzky R. F., Winter L. M., Fabian A. C., 2009, *MNRAS*, 399, 1553
- Vazdekis A., 1999, *ApJ*, 513, 224
- Winge C., Riffel R. A., Storchi-Bergmann T., 2009, *ApJS*, 185, 186
- Winter L. M., Mushotzky R. F., Reynolds C. S., Tueller J., 2009, *ApJ*, 690, 1322
- Wright E. L., 2006, *PASP*, 118, 1711

This paper has been typeset from a $\text{\TeX}/\text{\LaTeX}$ file prepared by the author.